BRILLOUIN SPECTROSCOPIC STUDIES OF XENON AND METHANE HYDRATES

BRUCE LLOYD WHIFFEN

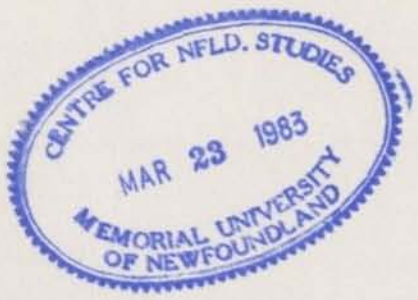
CENTRE FOR NFLD. STUDIES
MAR 23 1983
MEMORIAL UNIVERSITY
OF NEWFOUNDLAND

NOTICE

The quality of this microfiche is heavily dependent upon the quality of the original thesis submitted for microfilming. Every effort has been made to ensure the highest quality of reproduction possible.

If pages are missing, contact the university which granted the degree.

Some pages may have indistinct print especially if the original pages were typed with a poor typewriter ribbon or if the university sent us a poor photocopy.

Previously copyrighted materials (journal articles, published tests, etc.) are not filmed.

Reproduction in full or in part of this film is governed by the Canadian Copyright Act, R.S.C. 1970, c. C-30. Please read the authorization forms which accompany this thesis.

THIS DISSERTATION HAS BEEN MICROFILMED EXACTLY AS RECEIVED

AVIS

La qualité de cette microfiche dépend grandement de la qualité de la thèse soumise au microfilmage. Nous avons tout fait pour assurer une qualité supérieure de reproduction.

S'il manque des pages, veuillez communiquer avec l'université qui a conféré le grade.

La qualité d'impression de certaines pages peut laisser à désirer, surtout si les pages originales ont été dactylographiées à l'aide d'un ruban usé ou si l'université nous a fait parvenir une photocopie de mauvaise qualité.

Les documents qui font déjà l'objet d'un droit d'auteur (articles de revue, examens publiés, etc.) ne sont pas microfilmés.

La reproduction, même partielle, de ce microfilm est soumise à la Loi canadienne sur le droit d'auteur, SRC 1970, c. C-30. Veuillez prendre connaissance des formules d'autorisation qui accompagnent cette thèse.

LA THÈSE A ÉTÉ MICROFILMÉE TELLE QUE NOUS L'AVONS REÇUE

BRILLOUIN SPECTROSCOPIC STUDIES OF XENON AND METHANE HYDRATES

by

© Bruce Lloyd Whiffen, B.Sc. (Hons.)

A Thesis submitted in partial fulfillment
of the requirements for the degree of
Master of Science

Department of Physics
Memorial University of Newfoundland

May 1982

St. John's Newfoundland

To my mother and father,

for loving and caring

ABSTRACT

The technique of Brillouin Spectroscopy has been used to study the acoustic properties of clathrate hydrates. In particular, the longitudinal sound velocities in the hydrates of methane and xenon have been determined from artificially-grown polycrystalline samples.

A major part of this study involved an investigation of procedures for producing appropriate samples. This was met with limited success. Except for one xenon hydrate sample, the samples grown were somewhat opaque and milky. Nevertheless, light scattering studies were successfully carried out.

Since an exact measurement of the percentage cage occupancy was not feasible, the data are presented at occupancies of 75%, 90% and 100%. The dependency of the velocities on the occupancies arose through the Brillouin equation wherein the calculated hydrate indices of refraction were dependent on the occupancy percentage through the hydrate densities. Further, each velocity is expressed as a ratio relative to the longitudinal velocity in ice. Two sets of data for xenon hydrate are presented. The results are as follows:

HYDRATE	CAGE OCCUPANCY	HYDRATE/ICE VELOCITY RATIO	
METHANE	75	.894	
	90	.887	
	100	.880	
XENON	75	.775	.761
	90	.764	.750
	100	.753	.739

These data represent the first experimental velocity measurements for methane and xenon hydrates. The velocity ratios obtained through an extension of the only theoretical treatment performed to date (Whalley, 1980) are in approximate agreement.

ACKNOWLEDGEMENTS

To my supervisors, Dr. H. Kiefte and Dr. M.J. Clouter, for their assistance, guidance and leadership, I must express my most sincere thanks. The successful completion of this project was dependent not only on their excellent experimental facilities but, as well, on their expertise in this field.

I also wish to thank Mr. John Goosney for his assistance during the investigation of alternate methane hydrate growth procedures, and to Dr. S.F. Ahmad, for the use of his cryostat.

A final word of thanks to Miss Betty Miller for typing this thesis.

TABLE OF CONTENTS

LIST OF TABLES

LIST OF FIGURES

I. INTRODUCTION

I.1. Clathrate Hydrates

The purpose of the present work is to study the acoustic properties of some clathrate hydrates, in particular methane and xenon hydrate, by the technique of Brillouin Spectrosopy.

As introduced by Powell (1948), the word 'clathrate' identifies a structural formation in which the 'host' molecules form cages, each of which may accommodate at most one 'guest' molecule. Whereas the host molecules are chemically-bonded, the guest molecules of a true clathrate are simply trapped within the cages. While the presence of guest molecules is required to establish structural stability, not all cages are necessarily filled. For this reason, clathrates are non-stoichiometric.

Several substances are capable of forming the clathrate structure. Considerable attention, for example, has been given to the hydroquinone clathrates (Staveley, 1964). However, by far, the majority of experimental work has focused on those compounds whose clathrate lattice is composed of water molecules, i.e. the clathrate hydrates. Many gases, as well as some volatile liquids, may provide guest molecules (or hydrate former) to the hydrate lattice. Basically, the only restrictions imposed on the guest molecules are size (the largest cage is about 9 Å in diameter) and absence of a chemical interaction with the surrounding molecules. Some amine and salt hydrates are also known to exist. These, however, are more correctly labelled

'semi-clathrate hydrates' (Jeffrey, 1969), due to the strong interactions between the guest and host molecules.

I.1.1. Natural Occurrence

The first report of a naturally occurring hydrate deposit was made by Miller (1969), when a hydrate of air was found in an antarctic ice core. In 1970, Soviet scientists Chersky and Makogon (1970) reported that large fields of natural gas hydrates had been discovered, in the mid 1960's, under the permafrost in Siberia. A few years later, similar fields were found in Alaska and the Canadian arctic regions (Bily, and Dick, 1974). To date, however, these deposits have not been used as a source of natural gas, as doubts exist concerning the economic feasibility of such a project. Interest in natural gas hydrates, at least industrially, is more largely due to its formation above petroleum deposits, where its presence gives rise to a variety of problems related both to drilling and recovery operations. Hence, it is important that the acoustic velocities be known, in order to permit seismic detection of these materials.

It has been experimentally determined (Stoll, et al., 1971) that the acoustic wave velocity of a mixture of methane hydrate and sand grains is considerably greater than that of water-saturated sand. This phenomenon offered an explanation

for numerous observations of unexplained wave velocity increases in some regions of the ocean floor. Other factors could, of course, account for these observations. The authors (Stoll, et al., 1979) also raised doubts concerning the assumed similarity between possible naturally occurring ocean sediments containing gas hydrates and those produced artificially. For further reading see Hollister and Ewing.[1]

In a broader context, large quantities of methane hydrate are suspected of being present on Neptune and Uranus (Miller, 1961). Density measurements imply the presence of both water and methane on these planets and, by extrapolation of the dissociation pressure curves for methane hydrate, conditions appear to be favourable for its formation. Methane has also been detected in the atmospheres of Saturn and Jupiter and may similarly exist in the hydrate state. Comets may contain some methane hydrate as well (Whipple, 1951). Mariner probes have established that conditions are favourable for the formation of CO_2 hydrate in the ice caps on Mars (see Miller, 1973).

I.1.2. Structures I and II

With only a few exceptions, all clathrate hydrates form in one of two distinct structures, denoted Structure I (the framework of methane and xenon hydrates) and Structure II, (e.g. propane hydrate). As was previously mentioned, in both structures the water molecules form approximately spherical polyhedrons, or cages. They are, in order of increasing size, the pentagonal

---

[1]Hollister and Ewing, Initial Reports of the Deep Sea Drilling Project, U.S. Gov. Printing Office, pp. 9-50, 1973.

dodecahedron, the tetrakaidecahedron and the hexakaidecahedron; the first being present in both structures while the second and third are found in I and II respectively. A summary of their properties is given in Table 1. Diagrams illustrating the three cages and the Structure I lattice are found in Figures 1.1 and 1.2.

(i) Structure I

With reference to Figure 1.2, the 12 Å cubic unit cell of the Structure I hydrate is constructed as follows (Pauling and March, 1952). The smaller cages are located on each corner and at the center of the cube. Six additional water molecules per cell are required to complete the formation of the large cages. Each small cage is surrounded by twelve large cages, while each large cage lies adjacent to four small and ten large cages. Hence, two dodecahedra and six tetrakaidecahedra comprise each unit cell of forty-six water molecules, so that, with all cages filled, the empirical formula, for methane hydrate, say, is $8\ CH_4 \cdot 46\ H_2O$ or $CH_4 \cdot 5\ 3/4\ H_2O$. For guest molecules too large to be enclosed by the dodecahedra, the ideal formula is $6\ M \cdot 46\ H_2O$ or $M \cdot 7\ 2/3\ H_2O$.

The guest molecules known to form Structure I hydrates range in size from about 3.8 A in diameter to 5.5 A (Davidson, 1973). Although it is not known if smaller molecules will form Structure I, a lower limit is certainly required for sufficient interaction between host and guest molecules to

Table 1. Clathrate Hydrate Structural Properties

Property	Structure I	Structure II
Unit Cell Size (Å)	12	17
No. of Dodecahedra	2	16
No. of Tetrakaidecahedra	6	0
No. of Hexakaidecahedra	0	8
Cages per Cell	8	24
Water Molecules per Cell	46	136
Formulaes		
All cages filled	$M \cdot 5^3/_4 H_2O$	$M \cdot 5^2/_3 H_2O$[a]
Large cages filled	$M \cdot 7^2/_3 H_2O$	$M \cdot 17 H_2O$

Cage	Diameter (Å)[b]	Pentagonal Faces	Hexagonal Faces
Pentagonal Dodecahedran	5.2 and 4.8[c]	12	0
Tetrakaidecahedran	5.9	12	2
Hexakaidecahedron	6.9	12	4

Pentagonal Faces: 0-0-0 angle is 106°-115°[d]

Hexagonal Faces: 0-0-0 angle is 110° and 125°[d]

Structure I: average 0-0 distance is 2.81 Å[b]

Structure I: average 0-0 distance is 2.78Å[b]

a: Never Observed

b: Stackelberg, M. von and Mueller, H.R., Zeitschrift für Elektrochemie, 58, 25, (1954).

c: Minor Differences in Size Between Dodecahedra of Structures I and II.

d: Pauling, L., and Marsh, R.E., Proc. Nat. Acad. Sci., 38, 112 (1952).

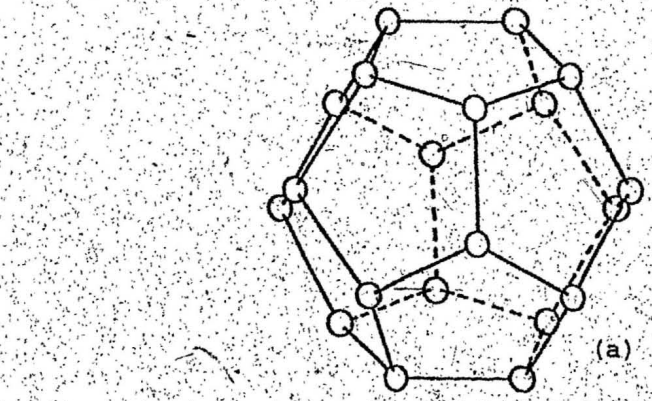

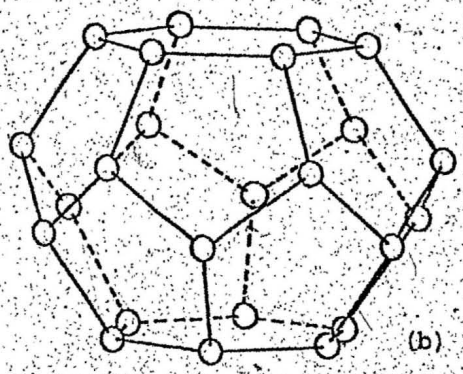

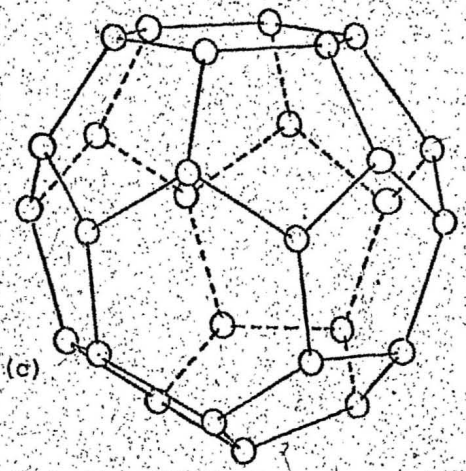

a: Pentagonal Dodecahedron
b: Tetrakaidecahedron
c: Hexakaidecahedron

Fig. 1.1 The Clathrate Hydrate Cages

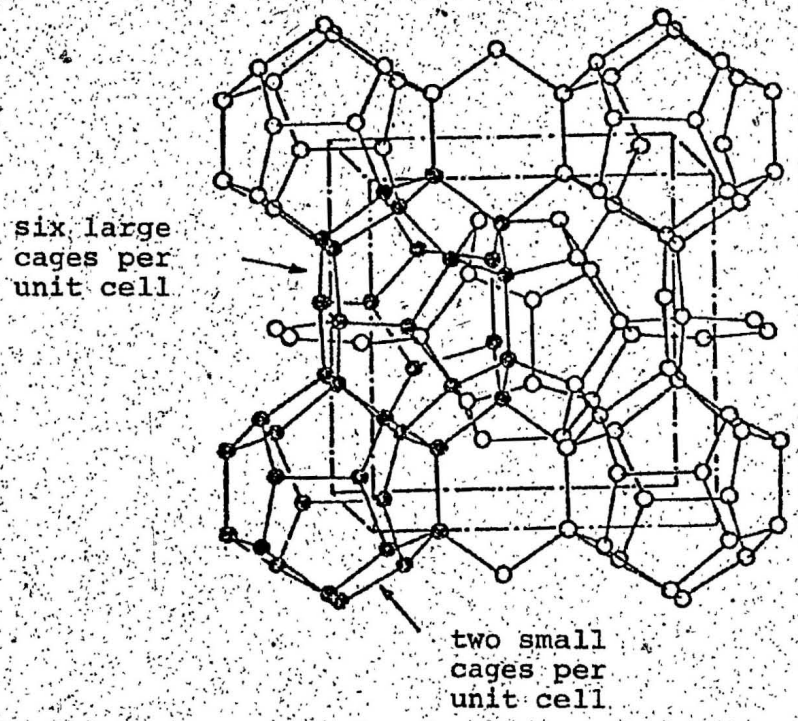

Fig. 1.2 Structure 1: Unit Cell (reproduced from Holder, 1976)

establish structural stability. The upper bound is determined, of course, by the size of the tetrakaidecahedron. Molecules larger than 5.1 Å in diameter are found only in these cages.

(ii) Structure II

The Structure II hydrate forms in the presence of guest molecules too large to occupy the cages of the Structure I hydrate. The 17 Å cubic unit cell is composed of 136 water molecules, arranged to form 16 pentagonal dodecahedra and eight hexakaidecahedra.

Guest molecules ranging in size from 5.5 Å to 6.7 Å in diameter form the Structure II hydrate. For a simple (i.e., one-component) hydrate, only the larger cages are occupied, since, otherwise, the guest molecules would be sufficiently small to form Structure I. It is possible, however, to fill the dodecahedra with a different type of molecule. For example, chloroform forms a Structure II hydrate with an empirical formula $CHCl_3 \cdot 17\ H_2O$. If, however, sufficient hydrogen sulfide is mixed with the chloroform before hydrate formation, the former will occupy the dodecahedra, with an ideal formula $2H_2S \cdot CHCl_3 \cdot 17\ H_2O$. This type of hydrate is called a double hydrate. In contrast, a clathrate formed when two or more types of molecules occupy both types of cages is known as a mixed hydrate.

I.1.3. Historical Review

The first clathrate hydrate to be grown in the lab was produced by Sir Humphrey Davy (1811), who discovered that an aqueous solution of chlorine gas became solid when cooled to about 4°C. Faraday (1823) attempted to determine its composition and reported an empirical formula of $Cl_2 \cdot 10\ H_2O$. He correctly noted, however, that due to the method used, the percentage of Cl_2 may have been underestimated. With the exception of a few isolated reports of hydrate formation (see Deaton and Frost, 1946), little experimental work was carried out until the late 1800's, when Villard and de Forcrand formed and analyzed a variety of gas hydrates.

The modern investigation of clathrate hydrates began when Hammerschmidt (1934) established that hydrate formation was the cause of clogging in natural gas pipelines. Although this problem was eventually corrected by removal of any water from the natural gas before entering the pipelines (Miller, 1973), a series of experiments was initiated to determine the pressure and temperature conditions necessary to avoid hydrate formation.

In addition to the relatively straightforward experiments on the determination of the P-T conditions of hydrate formation for various simple clathrates (e.g., Roberts, et al., 1940), particular emphasis was focused on pipeline conditions (Deaton and Frost, 1946), where several hydrate formers, in

varying concentrations, were present. More often than not, mole concentrations of the order of a few percent considerably altered the formation conditions. As well, the presence of 'help' gases, such as H_2S, and anti-freeze compounds (e.g. NaCl; Kobayashi, et al., 1955) were found to respectively aid and hinder hydrate formation. With the later realization that hydrates form one of two structures, experiments were performed to determine the equilibrium conditions between the two structures. A detailed account of this work can be found in Katz (1959).

The two most common clathrate hydrate structures were determined in the early 1950's. The Structure II formation was first proposed from model building by Clausen (1951), whose work was dependent on the supposition that the lattice consisted of pentagonal dedecahedra. The basis for this assumption were two-fold. First of all, the pentagonal angle for the model (108°) was very close to the tetrahedral angle ($109\frac{1}{2}°$). Secondly, the cage size appeared to lend itself to occupancy by the smaller guest molecules. His assumption proved to be valid, and laid the groundwork for the construction of Structure I by Pauling and Marsh (1952) a year later. M. von Stackelberg (1952), who had previously proposed the existence of two distinct hydrate lattices and had done much preliminary work, verified both structures from x-ray diffraction.

The 1950's also witnessed a growth in interest in the thermodynamic properties of the clathrate hydrates. Of particular

importance was the development of a statistical thermodynamic model by van der Waals and Platteeuw (1959). Using a Lennard-Jones 12-6 potential to describe the interaction between the guest and host molecules, the authors predicted the dissociation pressures for various hydrates. Although their calculated values were reasonably good for spherical and near-spherical guest molecules, the predictions for the diatomic molecules were, at best, correct only within an order of magnitude.

Both experimental and theoretical work on dissociation pressures was performed by Barrer and co-workers (1957, 1962, 1967), the last reference recording the first experimental determination of the dissociation pressures of the inert gas hydrates, including xenon hydrate. Other work (McKoy and Sinanoglu, 1963; Nagata, et al., 1966; Tester et al., 1972) focused on the use of other potential functions.

In the 1970's Stoll and co-workers (1971) began experimental work on the acoustic properties of sediments containing gas hydrates. They reported a significant increase in the sound velocity of sediments after formation of the hydrate (from 1.85 km/s to a maximum of 2.69 km/s), thereby introducing a plausible explanation for the observation of regions of high wave velocity on the ocean floor. Several factors appeared to play a significant role in the measured velocity. These included the formation conditions (the gas was bubbled through the water-sediment mixture) and the age of the hydrate-containing sediment, as would be expected in view of the effect

of the rigidity of the sediment on the sound velocity. As well, the velocity appeared to decrease with increased temperature. However, this information was only deduced intuitively during the course of the experiment, because a systematic study of these effects was not performed. In a later work (Stoll et al., 1979) a significant reduction in the thermal conductivity of the sediment upon formation of the hydrate was reported.

A theoretical model (Whalley, 1980) proposed values for the longitudinal sound velocity of Structure I methane hydrate and Structure II propane hydrate as a ratio with respect to the longitudinal velocity in ice. With all cages filled, respective ratios of .939 and .945 between hydrate and ice were reported. The difference between the velocity of sound in porous rock filled with ice and with hydrate was also investigated.

Using acoustic techniques, Pandit and King (1981) determined both the longitudinal and transverse velocities of Structure II propane hydrate. From the two specimens obtained, longitudinal velocities of 3.18 km/s and 3.05 km/s and transverse velocities of 1.67 km/s and 1.74 km/s were reported. No systematic change in velocity was observed as either a function of temperature or pressure.

The results cited in the previous two paragraphs are discussed further in comparison with the present measurements in Sect. V.1.

I.1.4. Phase Diagram

The portion of the phase diagram for methane hydrate in the vicinity and below 0°C is shown in Fig. 1.3. The letters W, I, H, L and G respectively denote water, ice, methane hydrate, liquid methane and methane gas. The curve segments AQ and QB represent part of the dissociation curve, where the hydrate is in equilibrium with ice and water respectively. Water and ice exist in equilibrium along QC. This curve is not exactly vertical. The coordinates of the quadruple point, Q are -0.19°C and 26 bar. Here, methane gas, water, ice and methane hydrate are in equilibrium. Also shown is part of the equilibrium line (OD), between methane hydrate + liquid methane and hydrate + methane gas, ending in the critical point, D, at 191 K. This curve is nearly coincident with the coexistence curve for gaseous and liquid methane.

A slightly more complicated situation arises when the liquid-vapor coexistence curve of the hydrate former intersects the dissociation curve of the hydrate. In addition to Q_1, which corresponds to Q in the above case, a second quadruple point, Q_2, occurs at this point of intersection. At Q_2, the hydrate former in both the gaseous and liquid states, as well as water and hydrate are all in equilibrium. Usually, the dissociation curve for the hydrate beyond Q_2 is very nearly vertical.

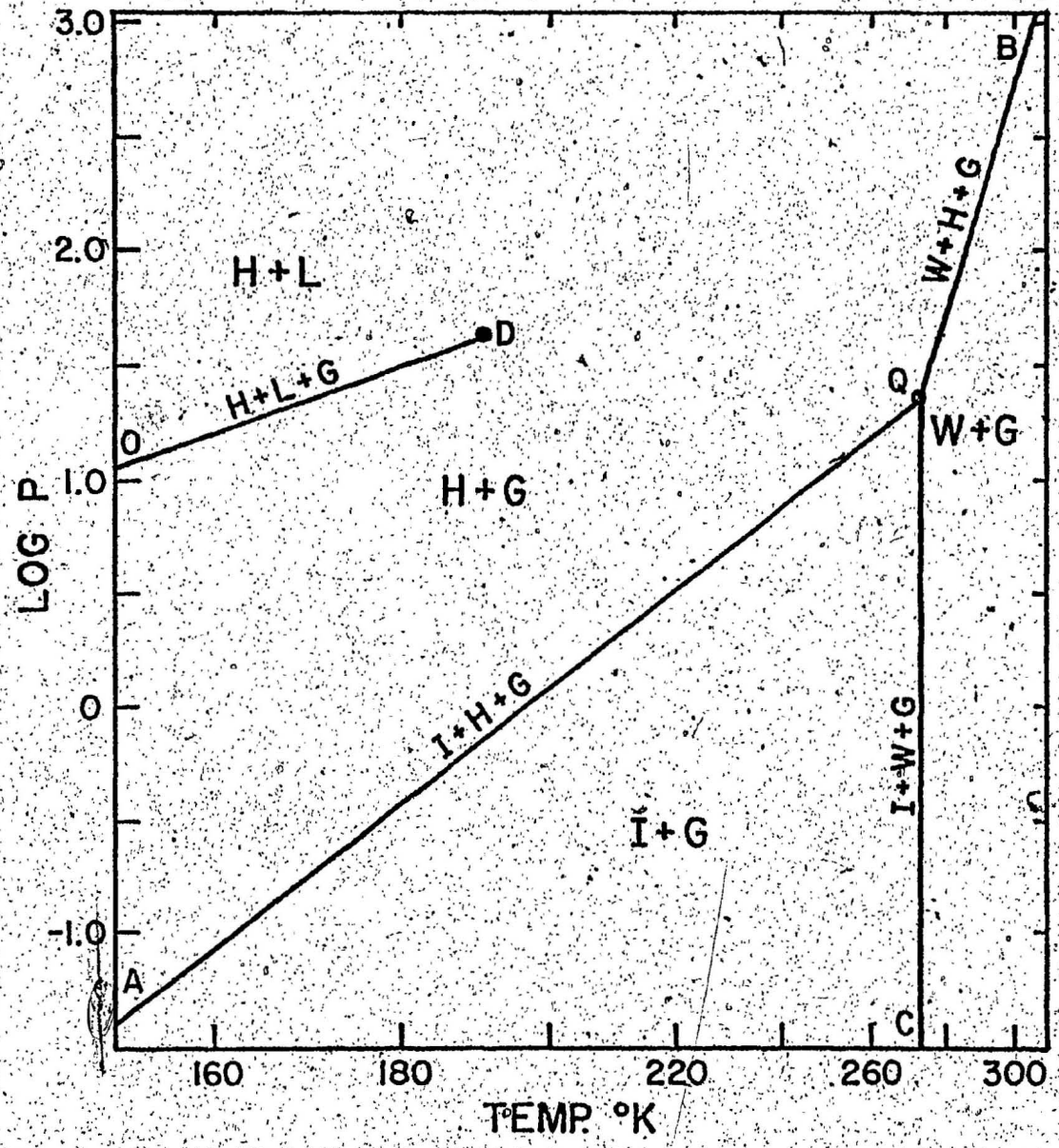

I: ice
W: water
H: methane hydrate
G: methane gas
L: liquid methane

Fig. I.3. Phase Diagram for Methane Hydrate (reproduced from Miller, 1973)

Respective experimental values of 1.5 bar and 1.15 bar for the dissociation pressure of xenon hydrate at 0°C have been reported by Barrer and Stuart (1957) and Platteeuw and van der Waals (1959), the latter in comparison with a calculated value, using a statistical mechanical model, of 1.0 atm. A more detailed analysis of the dissociation pressure was performed by Barrer and Edge (1967). Here, the experimentally determined decomposition pressures ranged from 4.90 cm Hg to 91.0 cm Hg through a temperature range of 211.2 K to 268.2 K.

I.2. Brillouin Scattering

Brillouin scattering can be viewed as scattering of light from spontaneous thermally-excited propagating density fluctuations, or elastic (acoustic) waves within the medium. The following classical model gives an intuitive understanding of the resultant Brillouin equation. More detailed discussions of Brillouin scattering may be found in Born and Huang (1954) and Benedek and Fritsch (1966).

Since the density fluctuations propagate in the form of alternate regions of compression and rarefactions in the medium, each elastic wave may be treated as a plane wavefront of velocity V, the elastic wave velocity. Consider two wavefronts, separated by distance s, incident, at angle $\alpha/2$ to two light rays, as shown in Fig. 1.4. The extra optical distance traversed by the second ray, r, may be expressed as

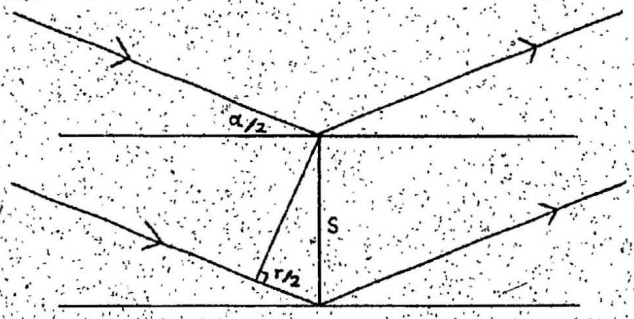

Fig. 1.4

2ns (sin α/2), where n is the refractive index of the medium. Time differentiation yields $\frac{dr}{dt} = 2nV \text{ (sin } \alpha/2)$, where V is the wavefront velocity. Here, $\frac{dr}{dt}$, the rate of change of extra optical distance travelled by the second ray as a result of the moving wavefront, may immediately be interpreted as a velocity of the light source.

The Doppler effect is well established in this regard. The frequency shift created by the light source velocity is

$$\Omega = \nu_{observed} - \nu_o = \frac{\nu_o V}{c} \qquad 1.1$$

in the non-relativistic limit (V<<c), where c is the speed of light, ν_o is the incident light frequency, and $\nu_{observed}$ is the scattered light frequency. Insertion of the term 2nV (sin α/2) into equation 1.1 yields

$$\Omega = \frac{\nu_o}{c} (2nV \sin \alpha/2) \qquad 1.2$$

or $$V = \Omega\lambda_o / (2n \sin \alpha/2) \qquad 1.3$$

where $\lambda_o\nu_o = c$. In this experiment, the scattering angle between the incident and scattered light was 90°. Equation 1.3 is called the Brillouin equation.

In general, for a crystalline substance, there are three types of acoustic waves, two transverse and one longitudinal, giving rise to three frequency shifts in a typical Brillouin spectrum.

II. EXPERIMENTAL APPARATUS

II.1. Optical Equipment

The primary optical components required to perform the light scattering experiments included: (1) a laser, to produce the intense (50-400 mW) highly monochromatic light beam necessary to probe the sample, (2) a Fabry-Perot interferometer, as a high resolution optical filter whereby the light scattered from the sample is separated into its frequency components, (3) a photomultiplier tube (PMT), as a light detection unit and (4) the data acquisition and stabilization unit (DAS), to store the information relayed from the PMT, and control the transmission frequency of the interferometer.

II.1.1. Laser

A Spectra-Physics model 165-08 Argon ion laser produced the highly monochromatic laser beam necessary in this experiment. The site of beam production, the plasma tube, positioned between a prism and flat mirror at the back end, and spherical mirror at the front, was held by an adjustable mount for precise alignment along the centerline of the mirrors. These mirrors, or optical cavity resonator, were supported by quartz rods, encased in an aluminum structure, to enhance rigidity and effectively eliminate thermal expansion effects. The externally adjustable prism served to select one of the two principal laser lines which are characteristic of the ionized Argon

medium (i.e., 5145 Å, 4880 Å).

Due to various effects within the laser, the laser emission spectrum is ordinarily broadened to about five GHz, at half intensity. This arises from the presence of several longitudinal, or axial modes, coexisting within the optical resonator, each of which satisfies the condition for constructive interference between the mirrors. Insertion of a Fabry-Perot etalon between the plasma tube and prism selected a single mode with an effective five MHz width. The 5145 Å line was used throughout the experiment.

The laser beam was first redirected through 90° by a beam steerer, consisting of two front-surface mirrors secured to adjustable mounts, to permit preliminary beam positioning. After passing through an aperture, the beam was focused at the cell site by a 25 cm focal length lens (L_3 see Fig. 2.1). A front-surface mirror (M), located below the cell and angled at 45°, redirected the beam for vertical passage through the cell. Both the lens and mirror positions could be fine tuned for selection of the desired beam path through the cell. Prior to cell entry, the beam passed through a quartz window, vacuum-sealed to the bottom cover of the cryostat, and a quartz plug at the cell bottom.

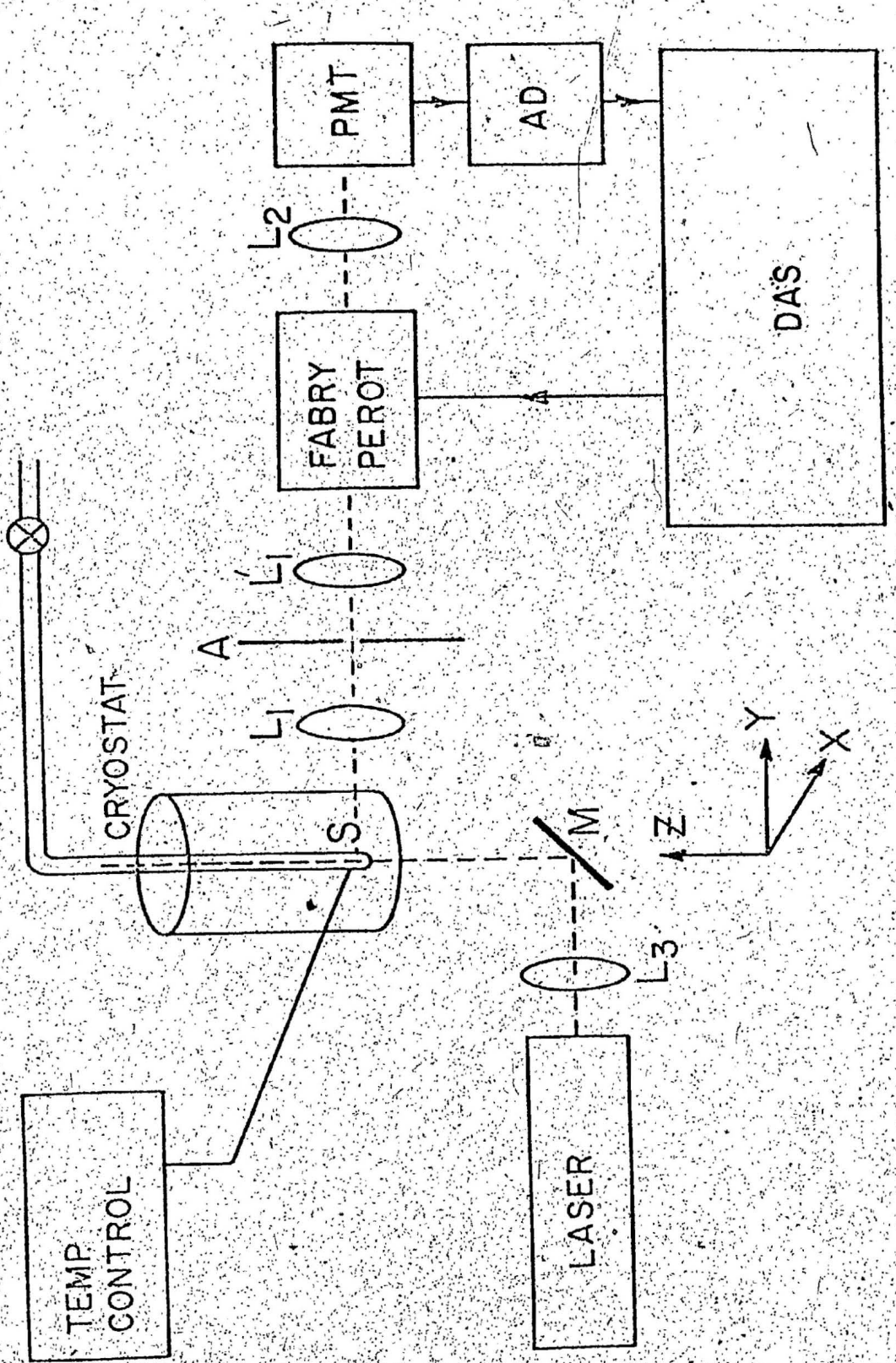

Fig. 2.1 Block Diagram of optical Setup

II.1.2. Spatial Filter

In the initial optical set-up, a single lens, located at its focal length from the cell, received the scattered light from the cell as a point source, thereby producing parallel rays for transmission through the Fabry-Perot interferometer (see Gammon, P.H., 1978). Soon after having begun to take spectra of the first methane hydrate sample, it was clear that the single lens was inadequate.

There were two fundamental problems with observing the scattered light from the hydrate. The relatively high degree of opacity of the hydrate to the laser beam caused intense parasitic scattering from the boundary region between ice and hydrate (see Sect. III.1). This, in addition to the fact that the region in which Brillouin scattering occurred (i.e., the hydrate region directly above the ice crystal) was small compared to the total effective region observed by the Fabry-Perot, yielded a large background, especially towards the shoulders of the central component, to the Brillouin spectrum. A spatial filter inserted between the cell and Fabry-Perot, considerably reduced the effectively observed cell region and consequently, the background and signal-to-noise ratio.

The spatial filter consisted of two lenses (L_1 and L'_1 separated by a 100 μm aperture (A). The scattered light, upon passing through the first lens (focal length = 10 cm), was focused and spatially filtered by the aperture. Both instruments

were secured to X-Y mounts for optical alignment. In particular, fine tuning of the lens allowed selection of the desired observation region. The second lens served the same purpose as the lens of the initial set-up. Positioned at its focal length (15 cm) from the aperture, it produced parallel rays for passage through the Fabry-Perot.

II.1.3. Fabry-Perot Interferometer

A Fabry-Perot interferometer serves to disperse light rays into its frequency components. Two parallel, highly reflecting plane mirrors (generally called 'plates'), separated by distance d and positioned normal to the light path, permit passage only of those photons corresponding to wavelength λ satisfying the constructive interference condition.

$$2d = m\lambda = \frac{mc}{\nu} \qquad m=\text{integer}=\text{order of interference} \qquad 2.1$$

In other words, only light is transmitted with an integral number of half-wavelengths equal to the plate separation. Minute, discrete changes in the plate separation produced by three piezoelectric elements, coupled with the appropriate light detection equipment, permit observation of the light over a desired frequency interval.

The Burleigh model RC-110 Fabry-Perot interferometer possessed high thermal and mechanical stability, vital criteria for minimizing the effects of the external environment on both

the constancy of the plate separation and on the high degree of parallelism necessary between the plates. These external effects commonly arise from mechanical vibrations, pressure (including acoustic), and temperature fluctuations. Mechanical stability was achieved via design symmetry, structural rigidity, and appropriate rubber and cork support mounting. Super-Invar, an iron-nickel alloy with a low thermal expansion coefficient, used almost exclusively in construction of the FP skeletal frame, enhanced thermal stability. The piezoelectric elements also contained low thermal expansion materials. These features are fully discussed in the technical manual for this Fabry-Perot.

The inner (near) surfaces of the plates were dielectrically coated for a reflection coefficient of .93. With a two inch diameter, they were rated by the manufacturer as being flat within a 25 Å variation. To avoid the possibility of constructive interference between the outer plate surfaces or in conjunction with one of the inner surfaces, each has been wedged a fraction of a degree. Hence, constructive interference could occur only between the inner surfaces of the plates.

The plate supports were mounted on three horizontal rods, positioned at 120° intervals. The rear support was translationally adjustable, permitting a maximum plate separation of 15 cm. A plate separation of 4.98 mm was measured for this experiment with the use of a strain-gauge and travelling microscope combination. Correct alignment of the plates, relative

both to the incoming scattered light and each other, was accomplished in part by manual adjustment of three triangularly-positioned screws controlling the front plate. Final adjustment was performed electronically, using the three piezoelectric elements connected to the rear plate. These elements also fulfilled the frequency scan requirements. By applying a common voltage to all three elements, the rear plate underwent a translational shift, thereby changing the plate separation and transmitted frequency. Of significant importance here was the requirement of a linear response to the applied voltage. Over five hundred step voltages were applied per scan before returning to the initial plate position, each step voltage corresponding to about a 25 Å change in the plate separation.

The free spectral range (FSR) of an interferometer is defined as the difference in frequency corresponding to a unit change in the order of interference, m (see equation 2.1). This accordingly, yields

$$(\nu_{m\pm1} - \nu_m) \equiv FSR = C/2d \qquad 2.2$$

In this experiment the FSR = 30.1 GHz. In the case of small changes (relative to d) in the plate separation, several orders of interference of light of the same frequency may be transmitted. At least two consecutive orders corresponding to the laser frequency were normally present, and any other frequency components (e.g. the Brillouin lines) were observed as being shifted by some fraction of the FSR from the laser maxima.

This (Brillouin) frequency shift was determined by a simple ratio calculation.

The contrast, C, of an interferometer is defined as the ratio of maximum to minimum transmitted intensity, or, in the case of a simple, one component (laser) spectrum, as the ratio of the central laser peak to the intensity observed at a shift of $1/2$ X FSR. Although, ideally, C would tend to infinity, this does not occur in practice, as 100% destructive interference is unachievable. For the Fabry-Perot used in this experiment, C was about 640 (see subsequent discussion of the finesse). By using the "triple-pass" feature (Burleigh model RC-22), however, the contrast is greatly increased. This required the use of two corner cube retroreflectors, placed respectively in front of and behind the front and rear Fabry-Perot plates. Each retroreflection caused a slight lateral shift of the beam (normal to the light path) such that the light passed through the Fabry-Perot three times before emerging. Since the triple pass feature is identical to use of three series-connected Fabry-Perots the theoretical contrast is tripled, with a resultant value of better than 10^8. In practice, contrasts of about 10^6 were achieved.

The finesse of a Fabry-Perot is defined as the ratio of the free spectral range FSR to the instrumental line-width, $\Delta\nu$, (full width at half maximum),

$$F = FSR/\Delta\nu \qquad 2.3$$

For single-pass operation, the theoretical finesse, F_1, for this Fabry-Perot (see the Burleigh Tech Memo for RC-22 Multipass) is determined from

$$1/F^2 = 1/F_r^2 + 1/F_f^2 \qquad 2.4$$

where F_r (Reflectivity Finesse) $= \frac{\pi\sqrt{R}}{1-R} = 43$

and F_f (Figure Finesse) $= n/2 = 100$

R (= .93) is the reflectivity of the Fabry-Perot plates and m is the rated plate flatness, $\lambda/200$ for $\lambda = 5000$ Å, giving $m = 100$. The theoretical single pass finesse, then, is 40, from which the single pass contrast, $C = \frac{4F_1^2}{\pi^2}$ was calculated to yield a value of 640. For multipass operation, F_1 must be multiplied by $(2^{1/P} - 1)^{-1/2}$ (where p is the number of passes through the Fabry-Perot) to yield a triple pass finesse of 78. The observed finesse, however, was usually about 50-60.

Prior to recording spectra, it was necessary to align the Fabry-Perot. This was achieved by, first of all positioning the interferometer such that the beam of a Helium-Neon laser was reflected back on itself from the rear F-P plate. The He-Ne beam defined the optic axis of the system, this being the axis along which observation of the light scattered from the cell occurred. Adjustment screws attached to the front plate were then used to produce parallelism between the two plates in the single beam (as distinct from spatially separated multiple reflections) from the Fabry-Perot. Upon repeated scanning of

the F-P plates, more enhanced parallelism was achieved when a single flashing spot emerged from the interferometer, as indicative of near complete constructive and destructive interference. Further alignment was achieved from light focused on and scattered from a card placed at the cell sight, using the beam of the Argon laser. The bias voltage applied to the piezoelectric drives of the rear plate was then adjusted. Finally, extremely sensitive tuning of the bias voltages was required after shifting to triple pass.

II.1.4. Photomultiplier Tube

After passing through the Fabry-Perot, the light was focused with a 100 cm lens (L_2) held by an X-Y mount, onto a "pinhole" aperture (diameter 400 μm) placed directly in front of the photomultiplier tube (PMT). In focusing the scattered light, only those photons travelling parallel to the optic axis entered the PMT. Acceptance of photons travelling at a slight angle to the optic axis, and hence passing through the Fabry-Perot at a different plate separation than those of the same wavelength travelling parallel to the optic axis, would have resulted in a broadening of the central components and reduction in the finesse. In selecting the pinhole size, a compromise was reached between the simultaneous requirements of (1) minimizing the acceptance angle and (2) collecting a sufficient amount of the scattered light. The thermoelectrically-cooled photomultiplier tube (Electro-optical Div. ITT,

model ITT FW 130) generated a photopulse, relayed to the DAS-1 via an amplifier-discriminator, (AD) for each photon received. Its dark count was less than one count per second.

The optical assembly from the aperture of the spatial filter to the PMT was enclosed in a black styrofoam box, covered in black cloth. With the room lights off no measurable stray light, relative to the dark count, entered the PMT.

II.1.5. Data Acquisition and Stabilization Unit

The Burleigh Data Acquisition and Stabilization System (DAS-1) served in accumulating and hence displaying the intensity of the light transmitted by the Fabry-Perot versus channel number or transmitting frequency. The Fabry-Perot plate separation was controlled by the DAS. Additionally, the DAS supplied voltage corrections to the piezoelectric elements connected to the rear plate of the FP to correct for drift and misalignment of the FP plates.

Output data from the photomultiplier tube was stored in the multi-channel analyzer (MCA) of the DAS. Although consisting of 1,024 channels, only one-half, or 512 channels, was utilized, the other half being used for storage and comparison with the previous spectra. A master clock, synchronized to the ramp waveform, swept through these channels in a manner equivalent to the sweep of the FB plates by the waveform. Thus, channel one corresponded to the initial plate position, channel two to the first displacement, and so on. Data accumulation occurred

only at the channel corresponding to the plate separation at that time -- each photopulse registering as one count in this channel. Photon counting did not occur during restoration to the initial plate position. Equivalent responses to the waveform by the plate ensured a linear relationship between the channel number and plate separation change and, consequently, transmission frequency.

The time period spent per channel could be altered in steps of .01 ms from .01 ms/ch to 99.99 ms/ch. Generally a 0.2 ms/ch time period was used. An additional feature, known as the "segmented time base", permitted longer accumulation times in one or more specific regions of the spectrum. A digital adjustment designated the factor by which the channel time was to be increased (maximum 99X). This option proved indispensible for observing the very weak hydrate signals. For example, using the segmented time base on a fifty channel segment, at 50 X, meant that over 80% of the accumulation time was spent in that region.

The entire memory of the MCA was continuously displayed in graphic form on the cathode ray tube (CRT) of the DAS -- the x- and y- axes respectively denoting the channel number and the total number of photons transmitted. An intensified spot indicated the channel number and its respective count total and could be manually controlled to indicate any particular channel. A running total of the number of sweeps was given at channel zero.

Because of the very long accumulation times required to obtain the hydrate signal (up to a few days in some cases), minor unwanted fluctuations in both the FP plate separation and alignment invariably occurred. To combat this, the DAS utilized two internal functions, the drift stabilization and finesse optimization. Both employed application of small correction voltages to the PZT.

The drift stabilizer ensured that the central component appeared in the same channel at all times. Three markers, positioned at channels 245, 250, and 255, were chosen such that channel 250 coincided with the desired position of the peak of the central component. After each sweep, the DAS compared the number of counts accumulated during that sweep in channels 245-249 with those accumulated in channels 251-255. A larger number for one group of channels implied a drift of the central line in that direction. A small correction voltage was then applied equally to the three PZT, the sign of which was determined by the direction of the drift of the central component. Normally, the magnitude of the correction voltage was chosen such that a compromise was reached between the rate of drift and the possibility of artificially broadening the central line. In all spectra, the minimum correction voltage was adequate.

The finesse optimization function of the DAS, responsible for maintaining parallelism between the plates, applied independent voltages to each of the three PZT's. Markers were

positioned at channels 248 and 252 and determined the region of total count accumulation upon completion of each sweep. A complete cycle of the finesse optimization procedure required four sweeps of the MCA. After the first sweep, a test voltage was applied to the PZT's, so as to tilt the rear plate about the two vertical axes. After the second sweep, a comparison (between the sweeps) of the counts accumulated on channels 248 -252 determined the effect of the test voltage. A correction voltage of smaller magnitude than the test was then applied. The sign of the correction voltage relative to the test was determined by whether the test voltage increased or decreased the count total. The third and fourth sweeps involved tilting of the rear plate about the horizontal axis. In all cases, the test and correction voltages were set at their minimum values.

The drift stabilization and finesse optimization features of the DAS-1 allowed spectra to be taken for indefinitely long periods of time. This proved to be necessary for the present experiments.

II.2. Cryostat, Cell and Gas Handling System

II.2.1. Introduction

Generally, the signal-to-noise ratio for a typical Brillouin spectrum is maximized when a minimum amount of 'parasitic' scattering occurs within the substance being studied. This stray light commonly arises from imperfections,

such as cracks or bubbles within the substance and has the effect of increasing the background of the spectrum and reducing the acoustic signals through attentuation of the beam. Ideally, a single crystal lacking these imperfections is desired.

Prior to this work, clathrate hydrates had never been grown for the purpose of conducting Brillouin experiments, most studies having focused on the production of bulk quantities whose optical quality was of no consequence. In the initial phase of this experiment, various methods of growing methane hydrate were investigated. This preliminary stage was motivated primarily by the fact that the cell required (for a light scattering experiment) differed appreciably from those previously used for growing hydrates. In addition, it was hoped that via manipulation of the cell parameters, the growth procedure would be refined to obtain hydrates of satisfactory optical quality.

The search for satisfactory methods of growing methane hydrate involved a number of changes in the sample cell, cryostat and gas handling system. The final version of the sample cell and cryostat will be initially explained, to be followed by a discussion of the various gas handling systems.

II.2.2. Cryostat and Cell

The hydrate samples were grown at the bottom of a 10 cm long quartz tube, 1.5 mm i.d., 6.5 mm o.d., (referred to subsequently as the cell), which was open to a gas supply at the top end and enclosed by a quartz plug at the bottom (Figs. 2.2

and 2.3).

Temperature control of the hydrate site was accomplished using a thermoelectric module. This module produced a temperature gradient between its upper and lower surfaces proportional to the amount of current supplied to it. The upper surface was the heat sink and remained in contact with a continuous flow of a 50:50 mixture of water and methanol, supplied by means of a Lauda K-2/R laser cooler. The temperature of this mixture was normally set at 4.5°C, and remained constant within a fraction of a degree. The temperature of the lower surface could be varied from close to the heat sink temperature to about -15°C at a maximum current of three amps. Further cooling sometimes required, was obtained by resetting the Lauda cooler. Thermal contact at the cell was provided by a copper braid and brass clip clamped to the bottom of the quartz tube. Since the plug extended beyond the top of the brass clip, the entire cell remained visible.

The temperature of the cell was monitored by a Gallium Arsenide diode attached to the brass clip. The diode was supplied with a constant current of 10 μA and the voltage produced (as measured by a Lakeshore Cryotronics Temperature Controller, model DTC-500) varied approximately linearly with its temperature, hence providing a means of accurately measuring the temperature changes. Absolute temperature readings required calibration using the diode voltages at the freezing point of a water column within the cell. While spectra were being taken, the voltage corresponded to a diode temperature of -15°C at the cell bottom.

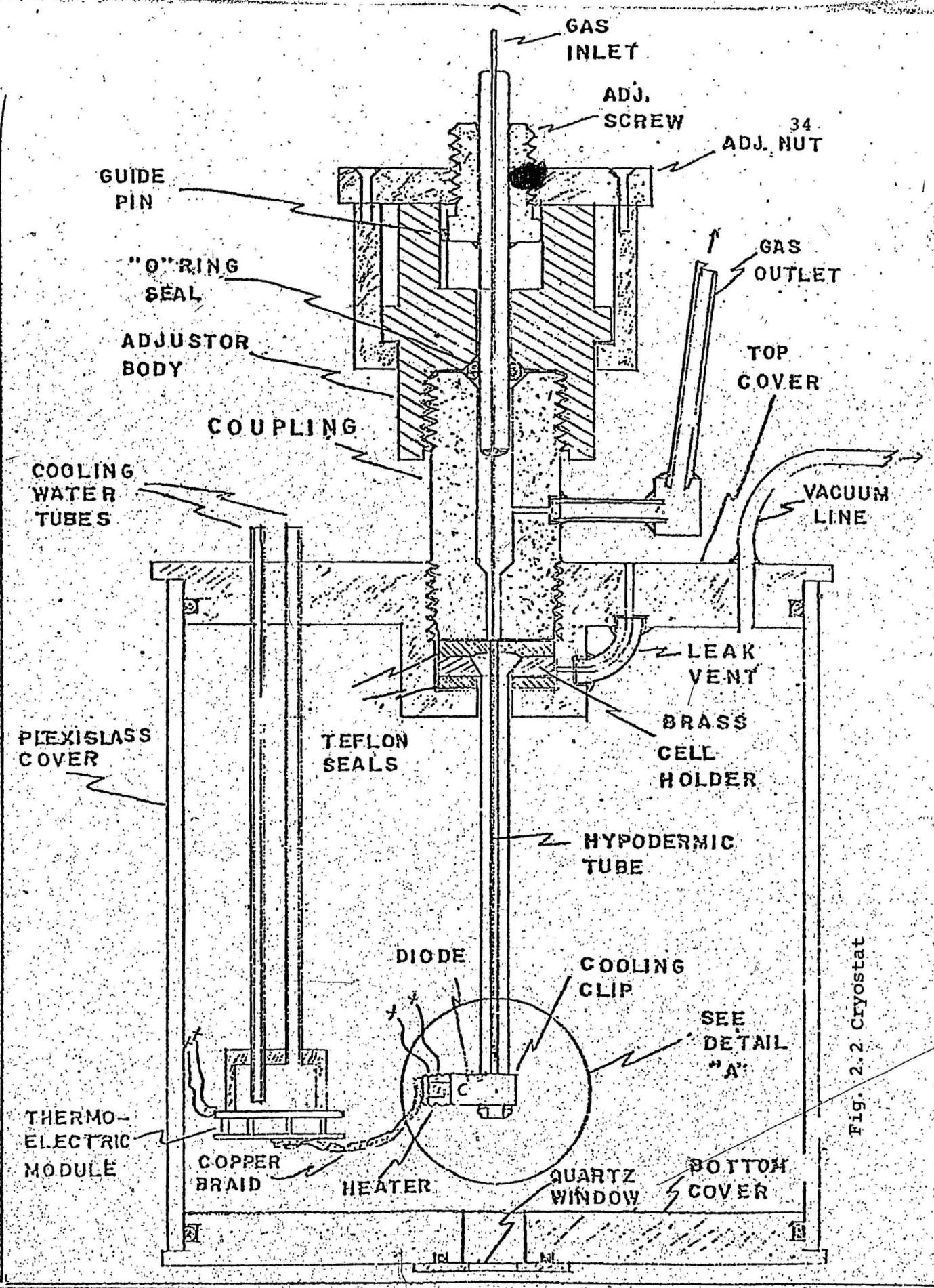

Fig. 2.2 Cryostat

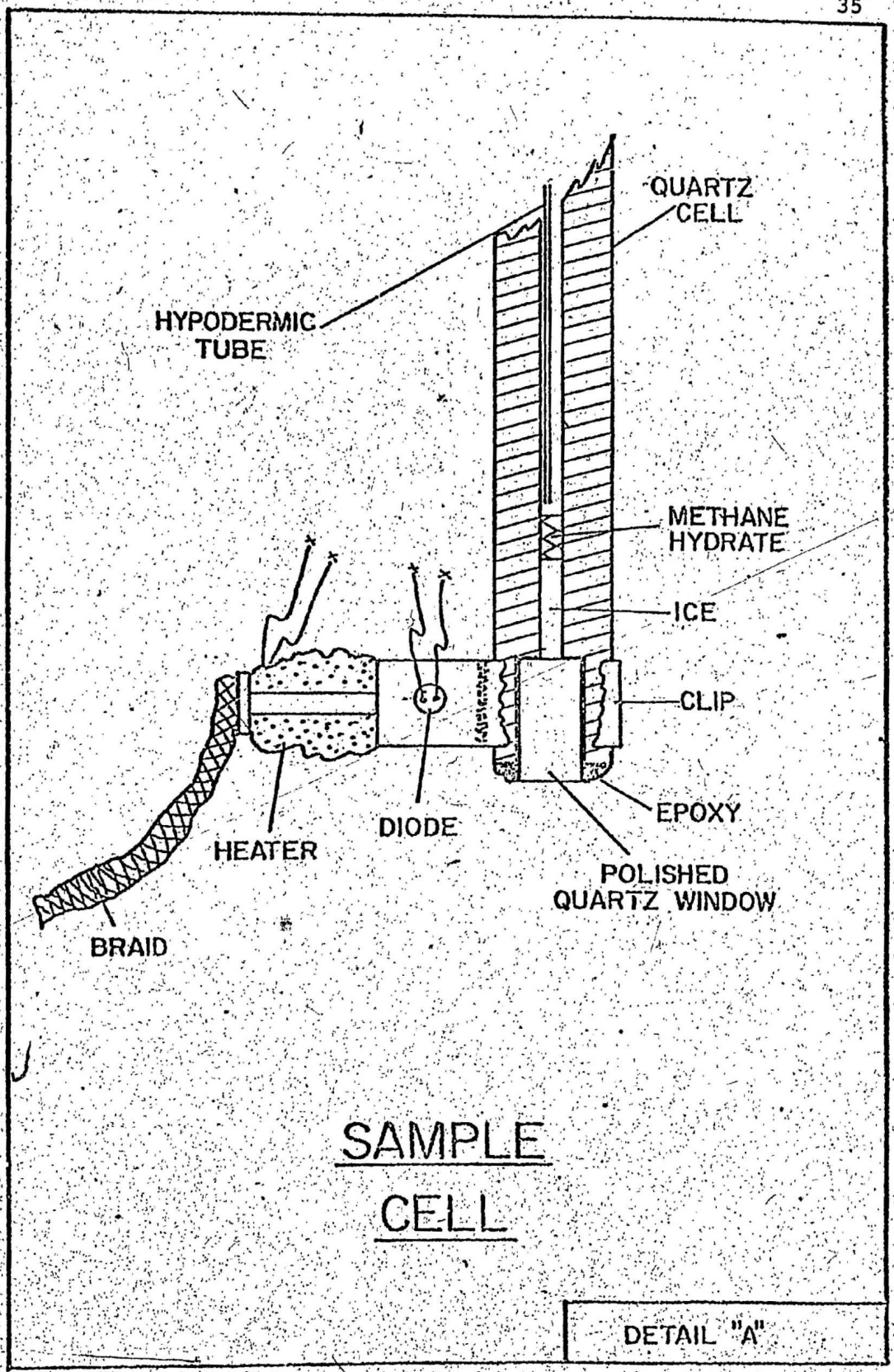

Fig. 2.3 Sample Cell

Based on the observed temperature gradient within the cell when forming ice samples a temperature of -10°C was assigned to the hydrate samples in these experiments. Although this estimate may be in error by as much as two degrees, it is of little significance, since the final calculations of the hydrate/ice ratios vary by less than 0.1% over a 5°C range.

The above assembly was housed in a cylindrical plexiglass tube (6 mm thick, 8.8 cm i.d.), O-ring sealed at the bottom with a plexiglass cover and, at the top by a brass cover. Through the latter passed the liquid coolant to the thermoelectric module, the electrical leads and the vacuum port. A quartz window in the bottom cover permitted passage of the laser beam through the quarz plug into the cell. The cryostat was evacuated to enhance temperature control, increase cooling power and prevent condensation of water on the cell walls.

II.2.3. Initial Setup for Preliminary Methane Hydrate Growth

In the initial set-up, the reservoir containing the doubly-distilled water supply was inserted as an extension to the $1/4$" copper tubing connecting the methane gas bottle to the cell. The first step in obtaining methane hydrate required evacuation of the system, including the removal of unwanted gases from the water reservoir. Once pumping had been stopped, the cell was cooled to about -5°C to permit condensation, at the cell site, of the water vapor from the reservoir. A supercooled column one centimeter in height could be obtained in a few

hours, from which an ice sample was obtained by further cooling. The system was then pressurized with methane gas, in the hope that the ice sample would serve as a catalyst for the formation of methane hydrate from the water vapor. Unfortunately, this did not occur -- at least not to a noticeable extent. Methane hydrate was formed, however, by inclusion of methane into the top surface of the ice crystal. This process took from several hours to over a day. Temperature and pressure variations of from $0^{\circ}C$ to $-15^{\circ}C$ and from 400 psi to 700 psi played no apparent role in affecting hydrate formation.

It was necessary at this stage to establish that the substances obtained were in fact methane hydrate samples. This was first indicated by its appearance, being similar to "packed snow" as described by Deaton and Frost (1946). As well, it remained intact, at sufficient pressure, after melting of the ice below, and dissociated only after the temperature or pressure was changed such that the formation conditions were no longer satisfied. Dissociation was particularly dramatic, with release of the methane continuing for several minutes.

II.2.4. Subsequent Gas Handling Modifications

Whereas under vacuum the water vapor from the reservoir readily condensed at the cell site, after introduction of the high pressure methane gas, hydrate formation from the vapor phase, or even condensation of the water vapor, was practically nonexistent. This immediately implied a reduction in water vapor concentration at the cell site, undoubtedly resulting from a low rate of diffusion of water vapor through the system. To correct this problem, the gas handling system was modified to permit a continuous flow of methane gas and water vapor through the cell (see Fig. 2.4).

The preliminary steps of gas flow after release of methane at 2000 psi from the methane bottle included passage through a pressure regulator, as a step-down to about 800 psi, a filter, and a metering valve used to regulate the flow rate. Flow then continued through the water reservoir, a second metering valve, and through a .5 mm o.d. hypodermic needle into the cell. At first, the position of the hypodermic could not be changed without disassembling the apparatus. Modifications then made utilized a screw mechanism (shown in Fig. 2.2) to allow variable height of the entrance of the gas mixture into the cell during the course of gas flow. Further discussion of hydrate growth will include only those attempts made using this modification.

After entering the cell, the gas mixture continued up to the top and passed out of the system through two, series-connected

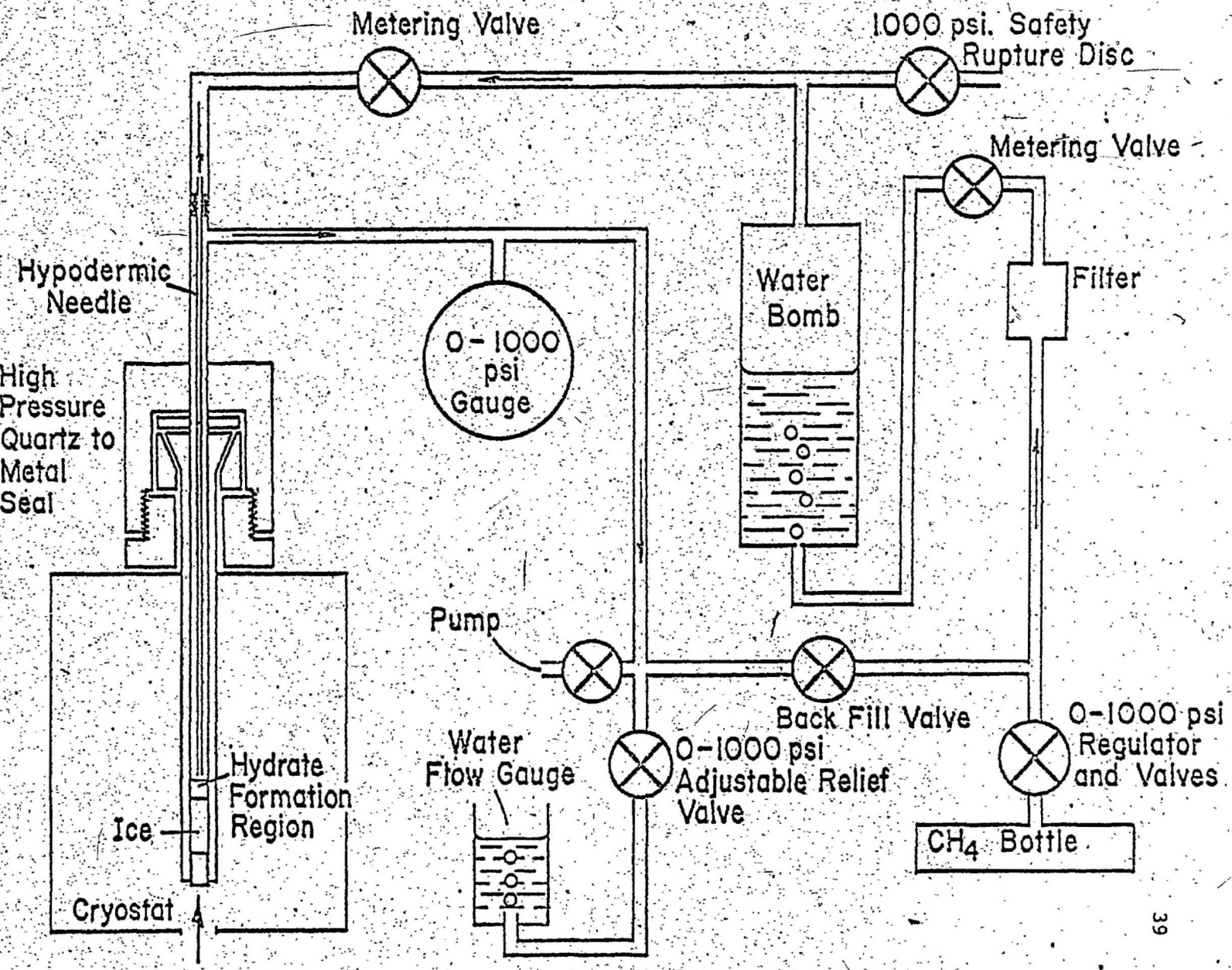

Fig. 2.4 Gas Handling System

relief valves. Each of these valves maintained a constant pressure differential between its entrance and exit, so that, after pressure build-up due to the gas flow, a sufficient amount of the gas mixture was automatically released to reduce the system pressure back to the desired value. Though the second valve was adjustable, settings of 400 psi and 250-300 psi were normally used, thereby maintaining 650-700 psi within the system. Upon exit from the second valve, the gas continued through a plastic tube into a water bottle, where the bubble formation rates indicated relative flow rates through the system. Flow rates in the range of 0.5-5 cm^3/s were typically used. To permit prefill of the system with methane gas, a back-fill valve to bypass the water reservoir was included. Other features of this system included a 1000 psi safety rupture disc, a 0-1000 psi pressure gauge, a vent to atmosphere, and a vacuum pump. All pertinent components were carefully cleaned to ensure the removal of foreign particles.

III. HYDRATE GROWTH AND RESULTANT BRILLOUIN SCATTERING

III.1. Methane Hydrate Formation

Essentially four cell parameters were adjustable in the course of growing the hydrate samples. They were the cell temperature, methane gas pressure, hypodermic tube height and gas flow rate. The effect of the presence of ice and water, as introduced into the cell before gas flow, was also investigated. In almost all cases where the hydrate formation conditions were favourable, samples could be obtained. The only significant effects of the cell parameters appeared to be on the rate of hydrate formation. All samples exhibited essentially the same appearance (i.e., as noted previously, that of "packed snow") and, were practically incapable of yielding Brillouin signals. The only major problem incurred with the setup arose from hydrate formation within the hypodermic, which resulted in tube blockage and stoppage of gas flow. This problem could only be alleviated by correct selection of the cell parameters; an unfortunate necessity which somewhat reduced the extent to which the parameters could be varied.

Although samples could be obtained with relative ease, very little can be said about the direct influence of each parameter. The methane gas pressure was not varied appreciably since it was felt that displacements (of the cell conditions) from the hydrate formation curve of the phase diagram could be more easily altered using the cell temperature. Generally it was found that

unless the temperature of the cell fell below at least -5°C (at 700 psi) water would condense in the cell. Although, at these conditions, methane hydrate is stable, condensation, as opposed to hydrate formation, was certainly not surprising, since a continuous flow of gas initially at room temperature into the cell undoubtedly caused a discrepancy between the temperature at the diode and that at the sample site. This discrepancy was, of course, a function not only of the gas flow rate but also of the point of entry of the gas mixture into the cell.

Initially it was hoped that with the hypodermic positioned just above the cell bottom, a very slow flow rate would result in hydrate formation on the quartz plug, after which successively raising the hypodermic height would allow increasing hydrate formation. It should be noted that a slow growth rate was desired not only because one would intuitively expect a better optical quality, but also because single crystals of other substances examined in this laboratory (e.g. ice, CO) were of best quality when grown slowly (typically several hours) from a seed. Although hydrate samples were obtained using this procedure, formation frequently occurred along the cell walls and on the hypodermic. Faster flow rates were generally accompanied by a more rapid hydrate formation. Blockage of the hypodermic became particularly prevalent in this case.

Gas flow over columns of ice and water was also investigated. As with initial attempts, where no gas flow was provided, hydrate of about 1 mm thickness formed in both cases in the upper

layer. Gas flow over this layer resulted in further hydrate growth on top of that already formed.

In the following sections a more detailed discussion of the growth of methane and xenon hydrate samples, as well as the resultant spectra are discussed, in chronological order.

III.2. Methane Hydrate Samples and Resultant Spectra

In keeping with the assumption that slowly grown hydrate samples would be of best optical quality, it was decided to first take spectra of a sample formed on the quartz plug from the flow-through method. A sample a few mm^3 in volume was grown at about -5°C and 650 psi using a flow rate of 0.5 cm^3/s. The cell (as in all subsequent cases) was then cooled to -10°C prior to taking spectra. After running several spectra, however, no acoustic signals could be obtained.

The most significant reason for immediately abandoning this method of hydrate growth was the presence of a thin film of epoxy within the cell extending just above the quartz plug. The question of whether or not this film eliminated the Brillouin signal cannot be answered. However, since the hydrate sample appeared to be relatively opaque to the laser beam (implying observable Brillouin scattering only in the hydrate region immediately above the quartz plug), blockage by the epoxy film appeared to be a distinct possibility.

The next, and all subsequent methane hydrate samples

studied were formed above an ice crystal by direct inclusion of methane gas into the ice. This, of course, eliminated the problem caused by the epoxy film, since now, light scattering from the hydrate occurred well above the quartz plug. At this stage, some changes to the optical setup were made as well. The spatial filter and glass refractor plate were inserted between the cell and Fabry-Perot -- the latter placed between the cell and L_1 and securely mounted allowing for rotation about the X-axis (Fig. 2.1). By rotating this plate, the sample site observed in the cell could be selected with precision. The plate thickness (2 mm) was selected such that the pertinent cell region could be viewed in its entirety by rotation of about 45° in each direction from the vertical position. For the particular hydrate growth method in question, it is apparent that the ice sample should be of the highest optical quality attainable in order to minimize attenuation of the laser beam before entering the hydrate. In addition, the observation of a strong Brillouin signal from the ice facilitated the accurate alignment of the scattering optics. It was consequently decided that the ice sample should be in the form of a single crystal.

The first stage in growing the ice crystal required gas flow through the water reservoir to the cell until the desired amount of water had condensed in the cell. A temperature of about 5°C (at 650 psi) permitted sufficiently rapid condensation while at the same time restraining hydrate formation. After evacuation of the system, including gas dissolved in the

water, the column was frozen, invariably as a polycrystalline sample. Conversion to a single ice crystal required melting of the sample from the top downward until only a thin film of ice over the quartz plug remained. It was, in fact necessary to reduce the thickness of this film such that it could not be seen by the naked eye -- its existence being inferred from beam scattering at the cell bottom. Unobstructed passage of the laser beam through this film was assured either by continued melting or, if necessary, by local heating (by the laser beam) of that portion of the film in the beam path. Once the beam could be clearly seen in the water column, the cell was recooled at a rate of about $^1/_4$ °C /hr (max.), until the entire column had been converted to a single crystal of ice.

Before hydrate growth commenced, fine tuning of the optical alignment was carried out. With the cryostat positioned such that the beam passed through the cell region closest to the Fabry-Perot, the front lens (L_1) of the spatial filter was adjusted in the x-direction to maximize the longitudinal ice signal. As a final step, the intensity of the ice signal was checked as a function of the orientation of the glass plate, both to ensure that the rotation angle did not adversely affect alignment, and as a preliminary estimate of the plate position corresponding to the ice surface (i.e., the region of hydrate growth), the latter being indicated by a dramatic reduction of the ice signal intensity.

After pressurizing the system to 650 psi with methane gas, the cell temperature was adjusted such that the temperature of the surface of the ice crystal was 0°C. Though previous trials had shown no noticeable temperature dependence of the depth to which methane hydrate formed within the ice crystal, it was intuitively thought that the instability of the ice lattice at this temperature would provide the most suitable condition for hydrate formation. Although some hydrate formed within an hour, the sample was left to allow continued growth for about one day.

Before running prolonged spectra, it was necessary to determine the glass plate orientation required to view the cell near the discontinuity between ice and hydrate. This region was selected on the assumption that observable Brillouin scattering would be strongest here. It was later verified that the hydrate signal grew weaker at higher hydrate regions, mainly as a result of attenuation of the beam. An added bonus when viewing the discontinuity was the presence of the ice signal.

Although the central component intensity increased dramatically (typically by a few orders of magnitude within a few degrees of plate rotation) as the observed cell position was scanned from ice to hydrate, the primary spectral feature used in deciding the best plate orientation for running prolonged spectra was the ice signal intensity. Initially spectra were taken in the ice region, i.e., at about 5-10° off that plate orientation which corresponded to a noticeable reduction in

the ice signal. Successive spectra were taken higher in the cell to a point beyond that where the ice signal disappeared.

Five methane hydrate samples were grown and studied, the basic procedure just described being followed in each case. Although no difficulty arose in obtaining strong ice signals, this was certainly not the case for the hydrate signal. Only two spectra (Fig. 4.18-19) produced hydrate peaks of significant intensity, respectively requiring five days and $1\frac{1}{2}$ days of total accumulation time. Numerous other spectra indicated the presence of "peaks" which have not been accounted for but could have been attributed to statistical fluctuations in the photon counts. The latter were not included in calculation of the frequency shift of methane hydrate. Further discussion of the growth and spectra of methane hydrate is found in Sect. V.2.

III.3. Xenon Hydrate Samples and Resultant Spectra

As with methane hydrate, xenon hydrate growth began after formation of the single ice crystal and optical alignment with respect to its longitudinal Brillouin signal. Growth of the first sample proceeded as follows. After evacuation, the system was pressurized to 41 psia with xenon gas at a cell temperature of -10°C. Hydrate formed in the first few minutes -- apparently both within the ice crystal as well as above. After a one-hour period, during which no further growth was observed, the hydrate temperature was varied from -15°C to

5°C over a period of about thirty hours. Although the final volume of hydrate was about twice the amount which had formed in the first five minutes, it is uncertain which temperature range was most conducive to growth.

Preliminary spectra were first taken to determine the approximate glass plate position required to view the cell near the ice-hydrate discontinuity. The first four spectra (taken at successively higher cell positions) are shown in Figs. 4.1-4.4. Figs. 4.2 and 4.3 contain the longitudinal hydrate signals. Spectra taken at higher positions included neither the ice nor hydrate signals. Upon returning to the regions at which the hydrate peaks had first appeared, only the ice peaks were evident.

Since the xenon hydrate peaks were not present upon returning back to the initial cell region in which they had first been observed, it was assumed that prolonged exposure to the laser beam had caused localized deterioration of the hydrate sample. That the beam's presence caused heating of the cell was evident from the observation that at laser intensities comparable to those used in obtaining spectra, the beam, within only a few minutes, was capable of melting the upper portion of an ice crystal. Since hydrate samples attenuated the beam to a far greater extent than the ice, localized destruction of the hydrate after several days of running spectra does not seem unlikely. Indications that the hydrate sample was being destroyed by the beam had been suspected while studying methane

hydrate. On a few occasions, hydrate peaks began to appear after only a few minutes but would become lost in the background after several hours.

In studying the subsequent xenon hydrate samples, all of which were grown using the basic procedure just described, an attempt was initially made to avoid destruction of the hydrate by reducing the beam intensity. While observing the ice region, the laser intensity was selected such that the ice signal was observable after a few minutes, thus necessitating several hours of accumulation time before the hydrate peaks would be observed. The observation that the hydrate peaks were evident, with the first sample, just prior to the reduction in the ice signal intensity which accompanied rotation of the refractor plate, was used in deciding the tilt of the refractor plate best suited to yield the hydrate peaks.

Although spectra were typically allowed to accumulate for several hours beyond the time at which the hydrate peaks would be expected to appear, nothing except the ice peaks was observed. Equally unsuccessful were spectra taken at different cell regions (both by rotating the plate and moving the beam) and, later, at higher beam intensities. This appears to suggest that the intensity reduction, coupled with the longer exposure times, was insufficient to eliminate destruction of the observed hydrate region.

Consequently, for the fifth xenon hydrate sample, even higher laser powers (300-400 mW) than that for the first sample

were used. It was, in this case, hoped that the laser intensities would be sufficiently intense to yield hydrate peaks before destruction occurred. Also, by taking successive spectra of the same region, it was anticipated that the intensity of the hydrate peaks would reduce with increased accumulation time, thereby offering evidence to regional hydrate destruction. Reasonable success was achieved in fulfilling these goals. Three independent regions were observed, either by moving the beam position in the cell or by permitting further hydrate growth into water. In each case, hydrate peaks were observed within the first few minutes.

The hydrate peaks for these spectra were relatively disperse and less intense than is conventional. This was to be expected, since it was necessary to terminate the spectra immediately after the presence of the peaks had been established. Further accumulation may have resulted in destruction of the probed region and loss of the hydrate signal. Unfortunately, this practice caused some problems related to determination of the peaks' channel positions. As the signals were not well defined, a somewhat larger error is to be expected for the channel displacement from the ice peaks than was the case for other spectra. These points become evident upon observation of the pertinent spectra (Fig. 4.5-4.11).

After running the first spectrum (for each region) for a time period considered sufficient to reveal the presence of the hydrate peaks, the spectrum was stopped, charted and

recorded in the memory of the DAS. Depending upon the circumstances, subsequent spectra were taken for equivalent time periods, charted, and added to the memory. A different region was observed after it was evident that the hydrate peaks were no longer present. Differences in the ice intensities for different regions were noted because of the sharp reduction in the ice signal near the ice-hydrate discontinuity.

The final xenon hydrate sample was by far the most successful, not only in terms of quantity and quality of the sample grown but also with regard to the resultant Brillouin spectra. Although the method used to grow this sample did not differ from the procedures previously followed, the results within the cell differed markedly. After introduction of the xenon gas into the cell, only a very small amount of hydrate formed within the surface of the ice crystal. Growth then proceeded upward to a height of about five mm, requiring a period of about three days from the time of introduction to the xenon gas. The cell conditions throughout were 45 psia and 0°C. As the entire system was evacuated prior to introducing the xenon gas, however, the water vapor required to form the hydrate grown above the ice crystal must somehow have been supplied from a quantity of water trapped within the system.

All previously grown methane and xenon hydrate samples had exhibited the "packed snow" description noted by Deaton and Frost (1946). However, the hydrate grown this time was somewhat more transparent, implying the existence of a sample

with only a few discontinuities relative to previous ones. Nevertheless, flaws within the sample resulted in far more Rayleigh scattering than in passage of the beam through the ice crystal.

A series of spectra (Figs. 4.12-4.17) was taken through the entire region of the cell, from within the ice crystal to the top of the hydrate sample. Upon dissociation of the sample, xenon gas release from the transparent hydrate appeared to be more intense and prolonged (almost one hour) than had been observed before.

IV. RESULTS

The spectral results obtained for xenon hydrate are discussed first, as the higher quality of these samples not only resulted in stronger hydrate signals, but also permitted a more thorough investigation of the differences between Brillouin spectra taken throughout the cell region. This process, performed for the first and last samples, provided a means for understanding the effects of the cell constituents on the scattered light (e.g., signal intensity) as well as determining the cell regions most conducive to yielding the hydrate signal. Following this, the average frequency shift difference between ice and xenon hydrate is determined for all but the final sample. The frequency shift calculation for the final sample is then performed independently, as these results were felt to be far more reliable. Discussion of the methane hydrate spectra follows that of xenon hydrate.

On the spectra shown in Figs. 4.1 to 4.19, R' and R" represent consecutive orders of the unshifted central component; i' and i", and h' and h" represent the upshifted (from R') and downshifted (from R") longitudinal components of ice and the hydrates, respectively. The elevated section at the centres of each spectrum is obtained by use of the segmented ramp feature discussed on page 29.

IV.1. Xenon Hydrate

IV.1.1 Sample 1: Discussion of Spectra

Once it had been established that a hydrate signal could be obtained from the first xenon hydrate sample, it was decided to investigate more closely the differences in spectra taken at different regions of the cell. Unfortunately, the results of this exercise were somewhat limited because, to avoid overloading the PMT, it was necessary to reduce the incident laser power for those spectra near the ice-hydrate discontinuity.

For purposes of comparison with subsequent spectra, a preliminary spectrum (Fig. 4.1) was taken of the ice crystal, with an accumulation time per channel of almost four minutes (237.5 s.). The background count rate was 2 cts/s per channel, of which about one-third is attributed to the dark count of the PMT. The signal level at the Brillouin peaks was 7 cts/s.

Prior to running the second spectrum (Fig. 4.2), the glass plate was rotated through about 10° (from 15° to 5° from the vertical), corresponding to a 0.2 mm height increase in the region of the cell observed. The pertinent spectral data are as follows: (1) accumulation time per channel = 738 seconds, (2) background count rate = 2.6 cts/s, (3) ice signal level = 8 cts/s, (4) hydrate signal level = 0.4 cts/s.

Surprisingly, the ice signal level actually increased, an unexpected result in view of the fact that the cell was now being observed closer to the hydrate sample. This would appear to indicate that the optics were more suitably aligned at this plate orientation. The background rate increased by about 25%, and undoubtedly resulted from the parasitic scattering, or Raman scattering (from the hydrate) at the ice-hydrate discontinuity. The count rate at the central Rayleigh line had doubled over the previous spectrum.

At this stage, before running the third spectrum (Fig. 4.3) the laser intensity was reduced because Rayleigh scattering from the hydrate in this region of the cell overloading of the photomultiplier tube. This was an unfortunate necessity, as comparison with the previous spectra is somewhat repressed. Nevertheless, the following data were recorded: (1) Accumulation time = 669 s, (2) background level = 1.9 cts/s., (3) ice signal level = 1.5 cts/s., (4) hydrate signal level = 0.07 cts/s. The reduction in the ice and hydrate signals, as well as their resultant poorer quality, is attributed to the reduced incident laser intensity. The ratio of the ice to hydrate rates remained the same.

A further reduction in the laser intensity was required before taking the fourth spectrum (Fig. 4.4): (1) Accumulation time = 711 s, (2) ice signal rate = .75 counts /s, (3) background rate = 1.7 counts /sec. Once again the ice rate was reduced from the previous spectrum. One would normally expect an

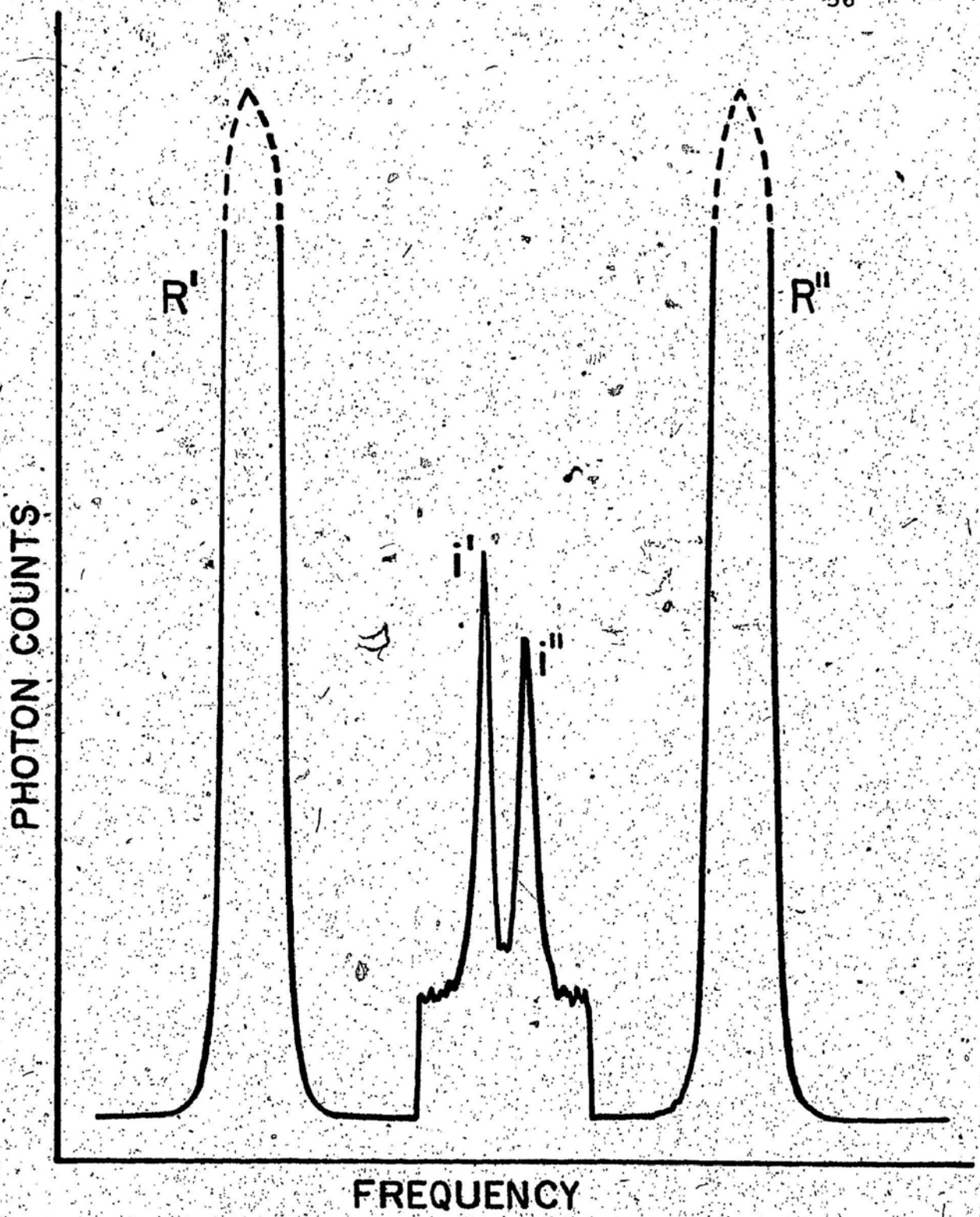

Fig. 4.1 Xenon Hydrate: Spectrum IA

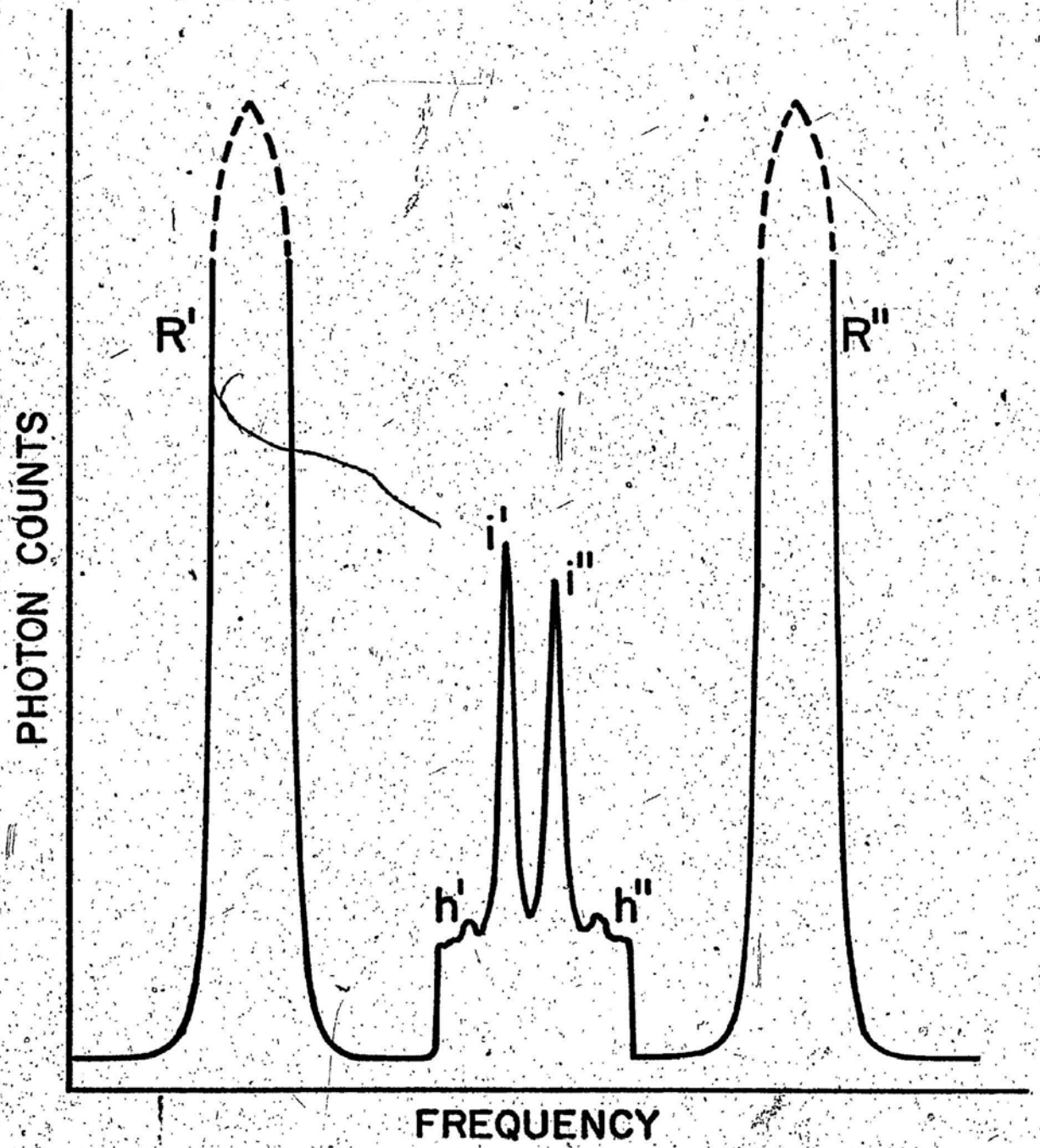

Fig. 4.2 Xenon Hydrate: Spectrum IB

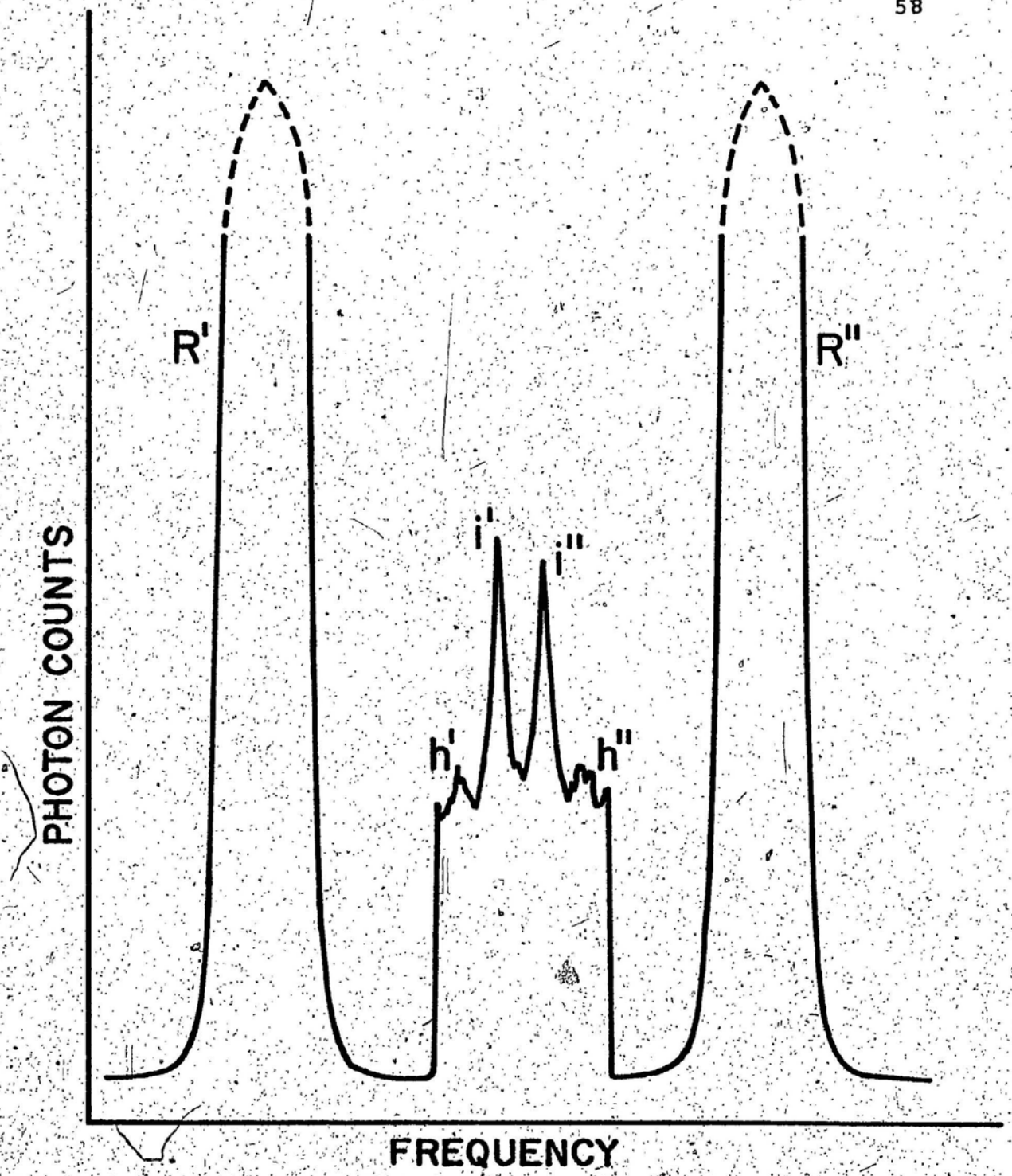

Fig. 4.3 Xenon Hydrate: Spectrum IC

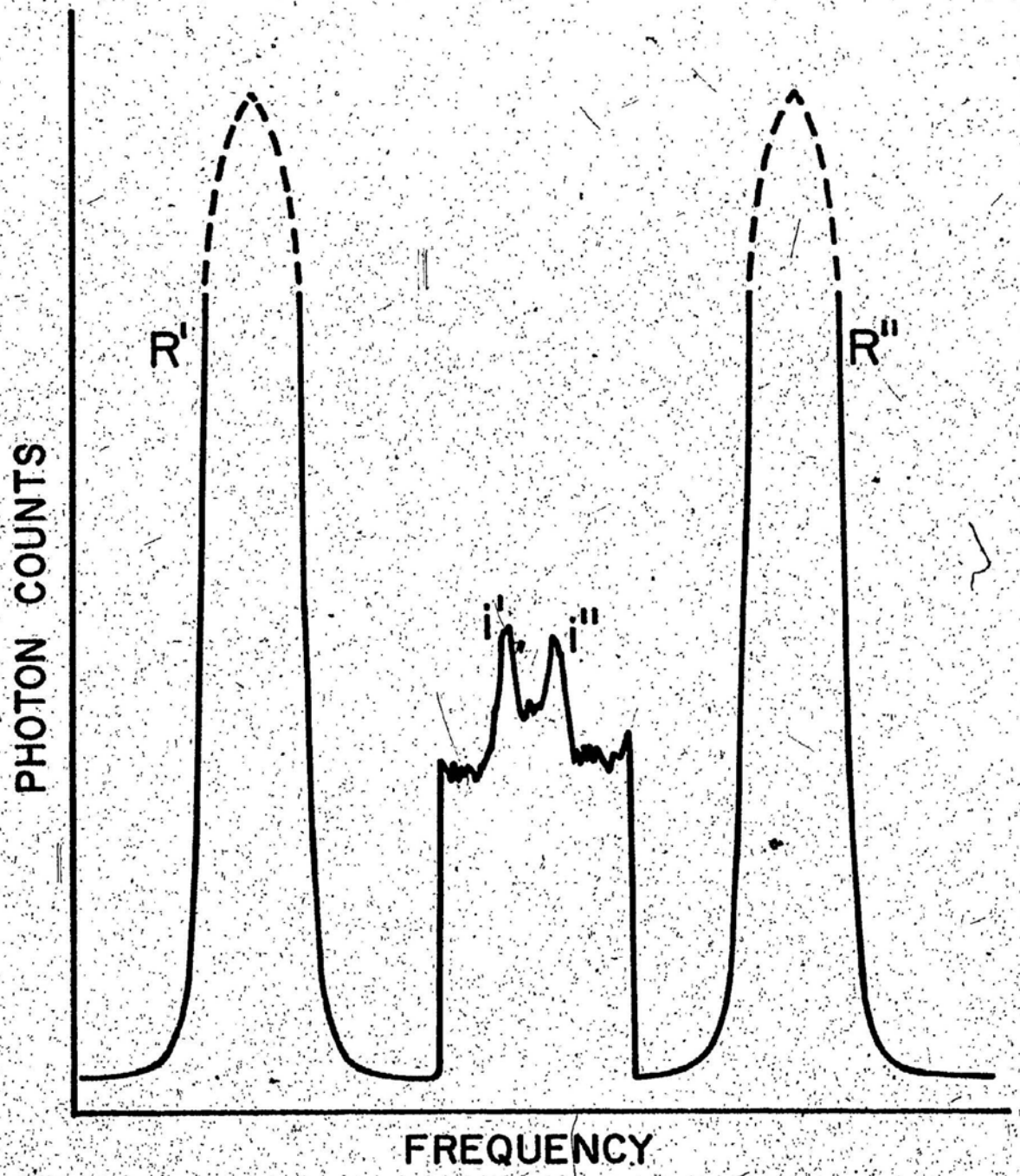

Fig. 4.4 Xenon Hydrate: Spectrum ID

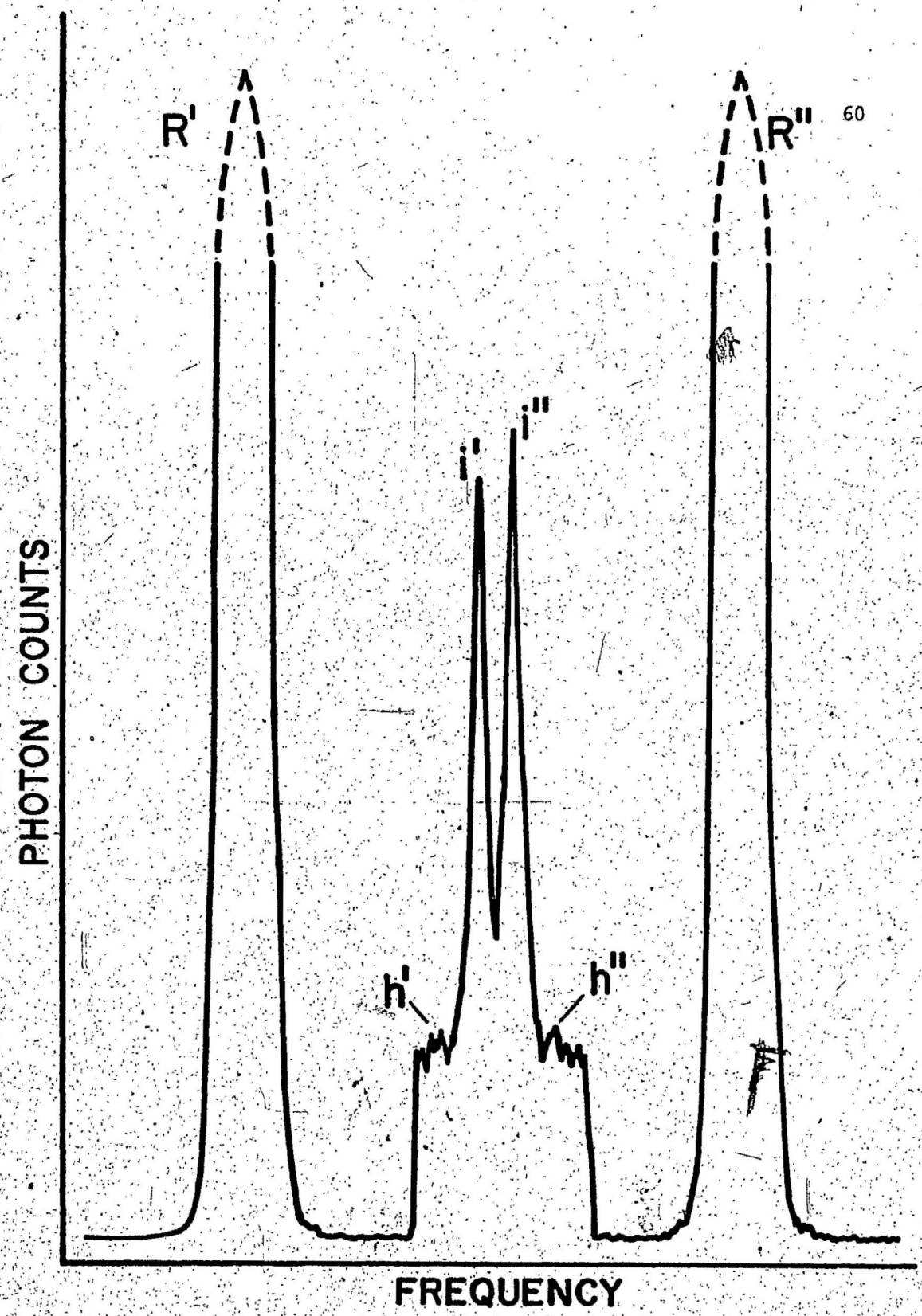

Fig. 4.5 Xenon Hydrate: Spectrum IIA

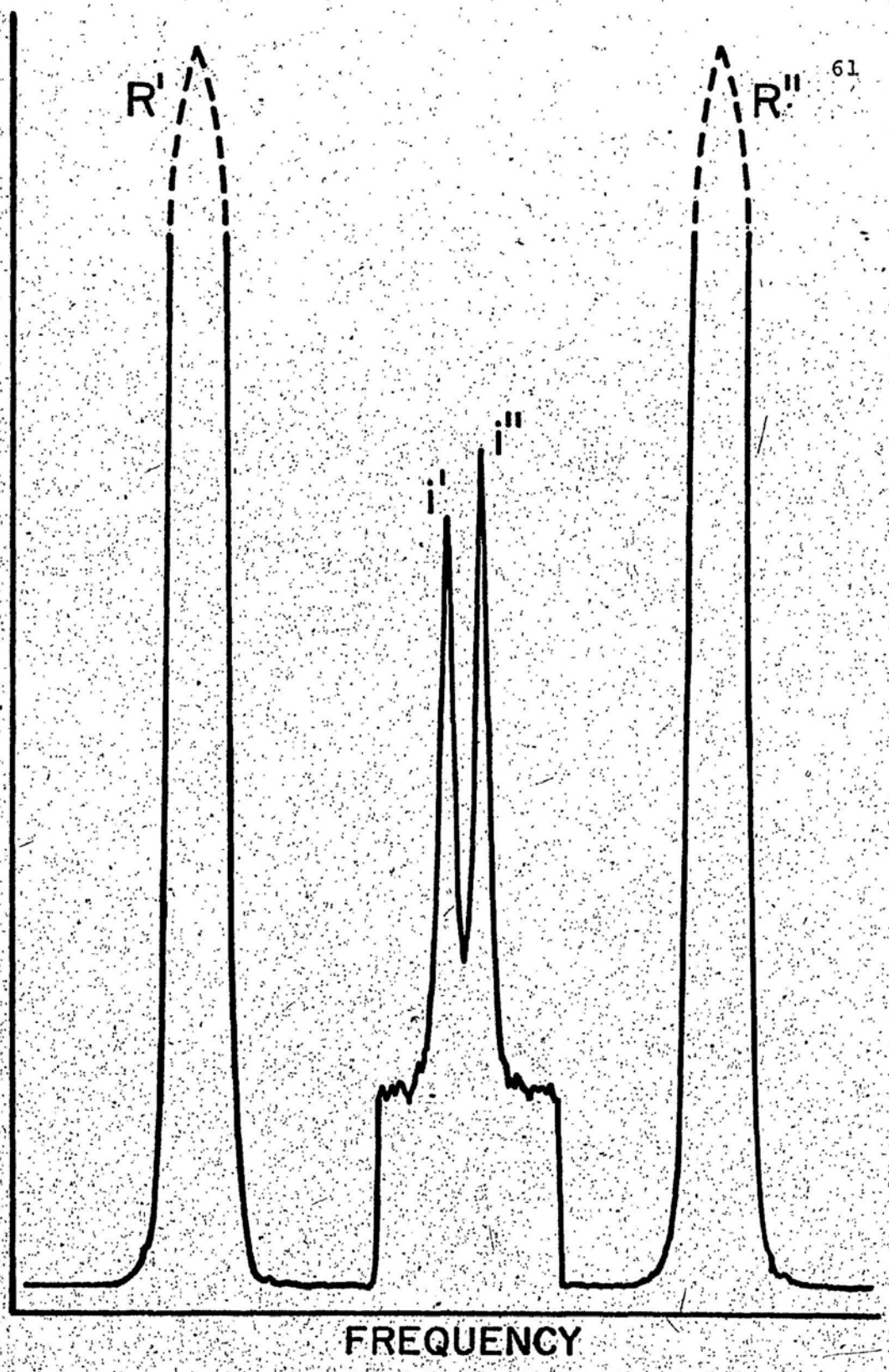

Fig. 4.6 Xenon Hydrate: Spectrum IIB

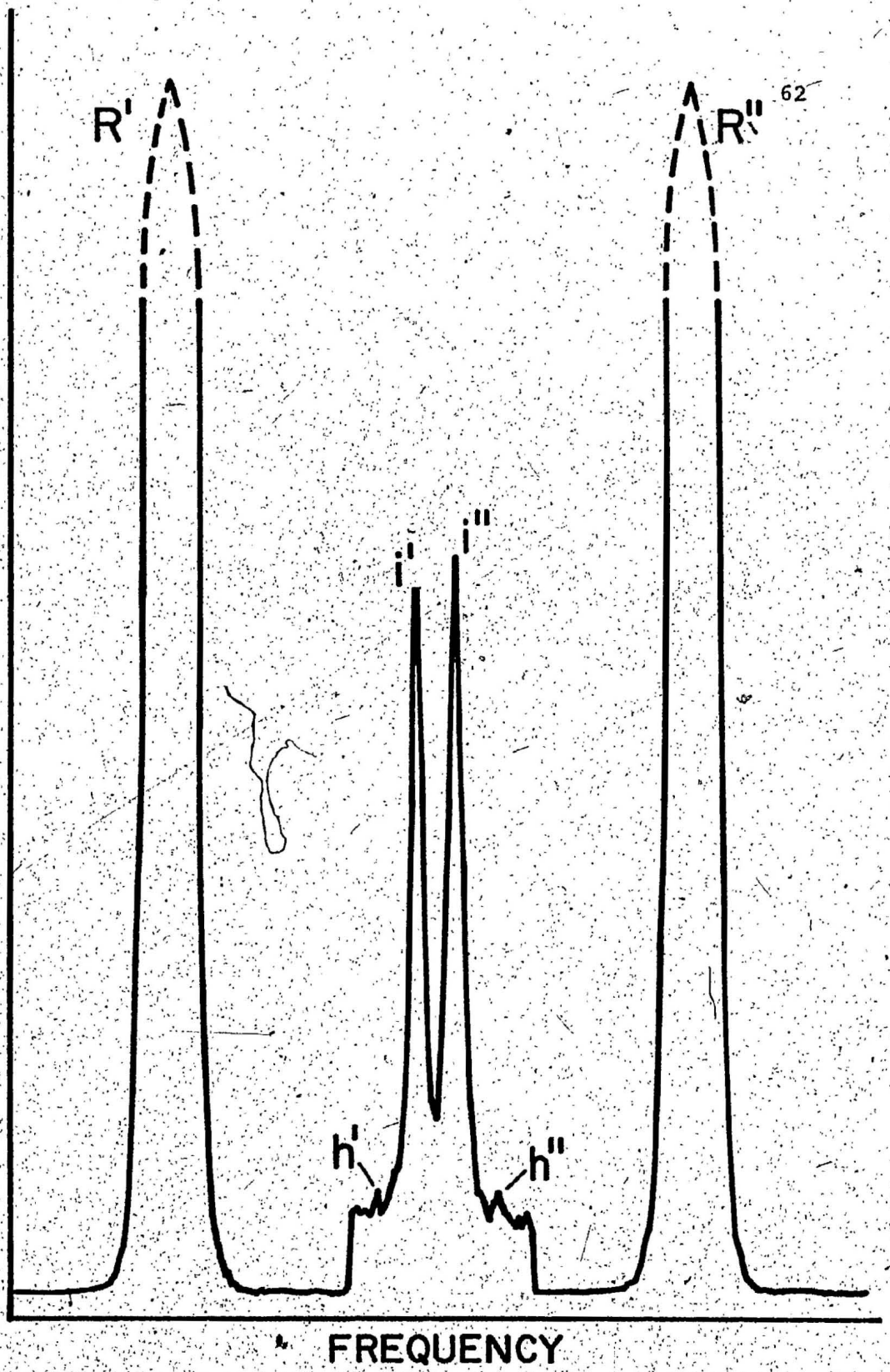

Fig. 4.7 Xenon Hydrate: Spectrum IIIA

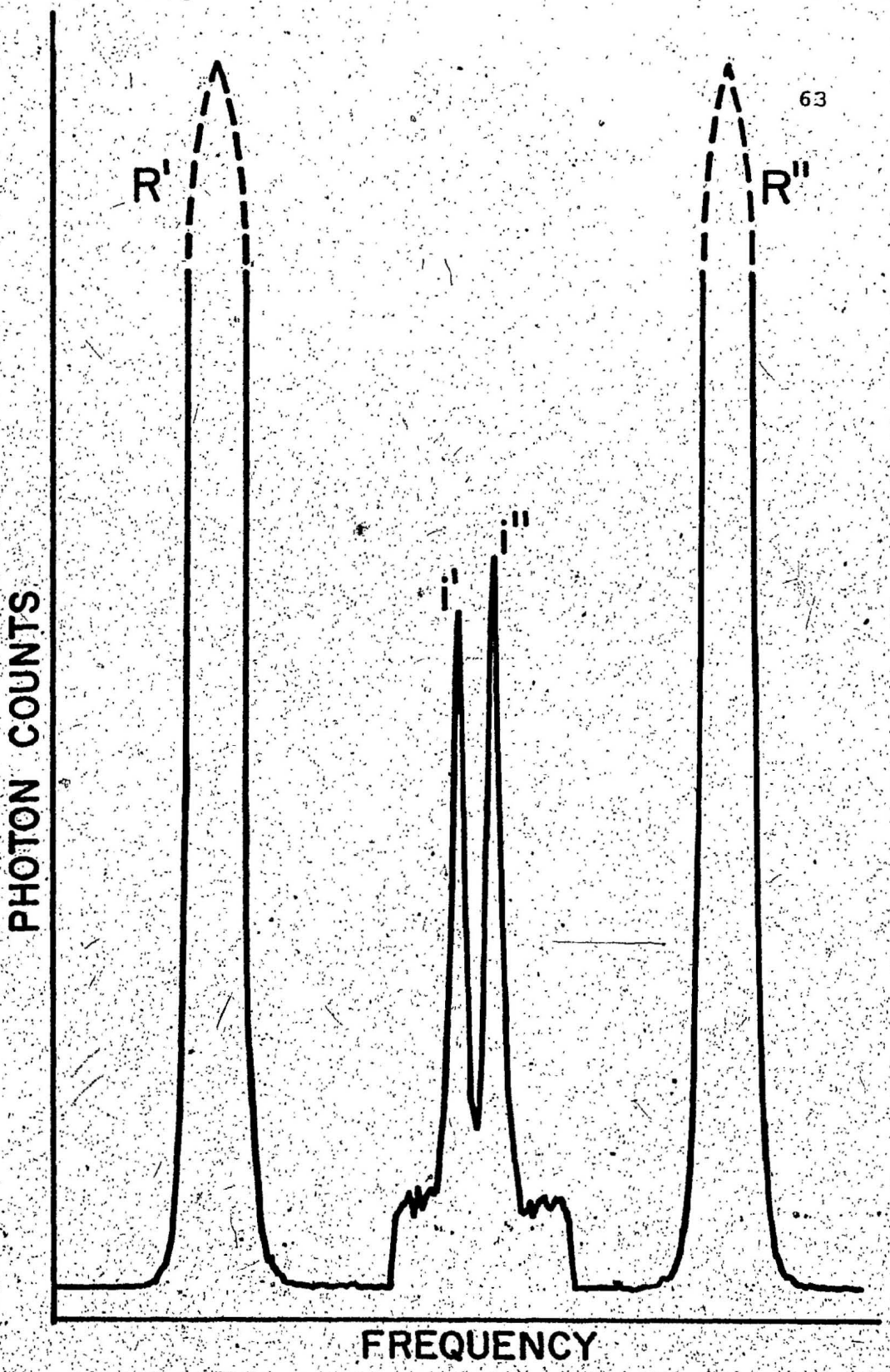

Fig. 4.8 Xenon Hydrate: Spectrum IIIB

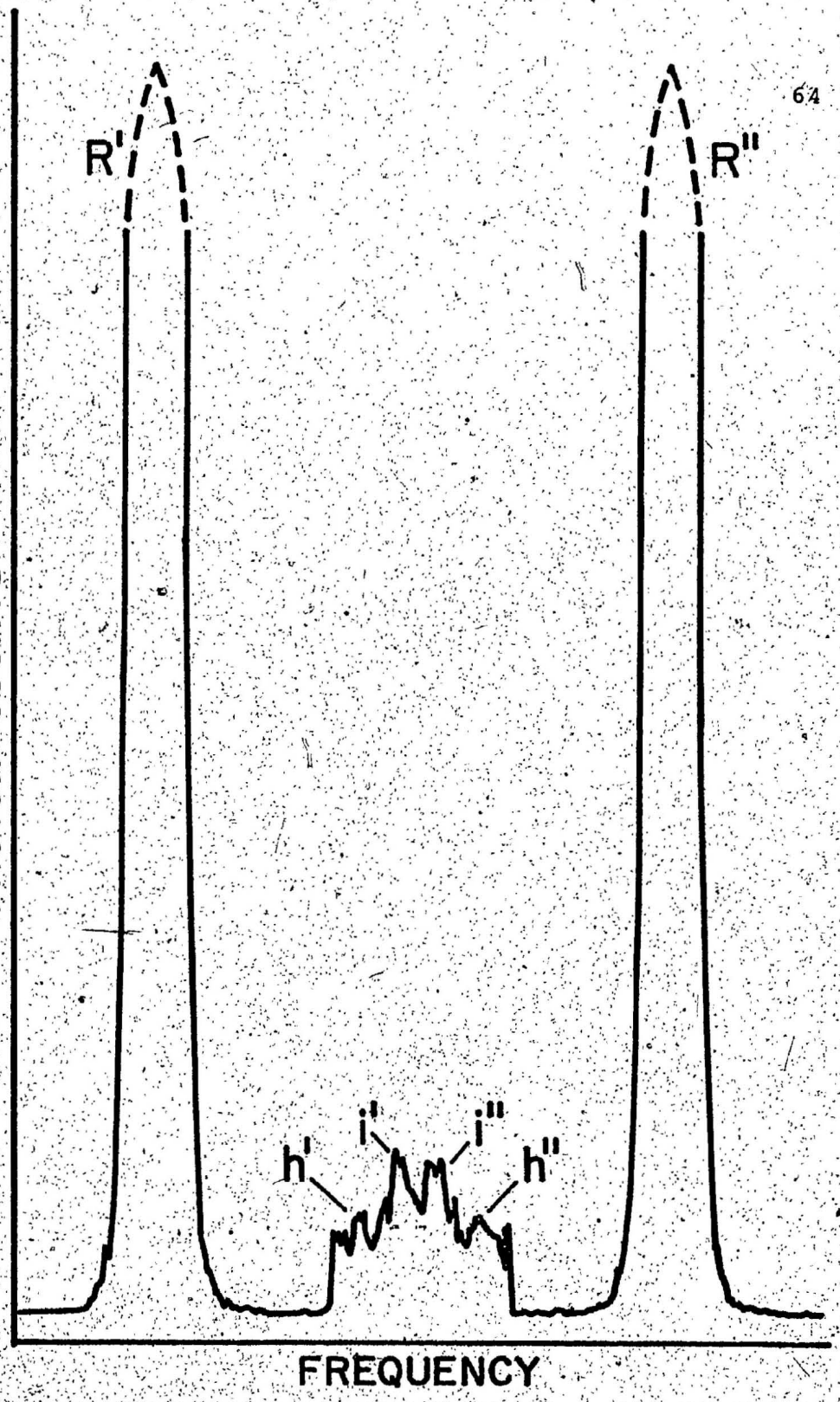

Fig. 4.9 Xenon Hydrate: Spectrum IVA

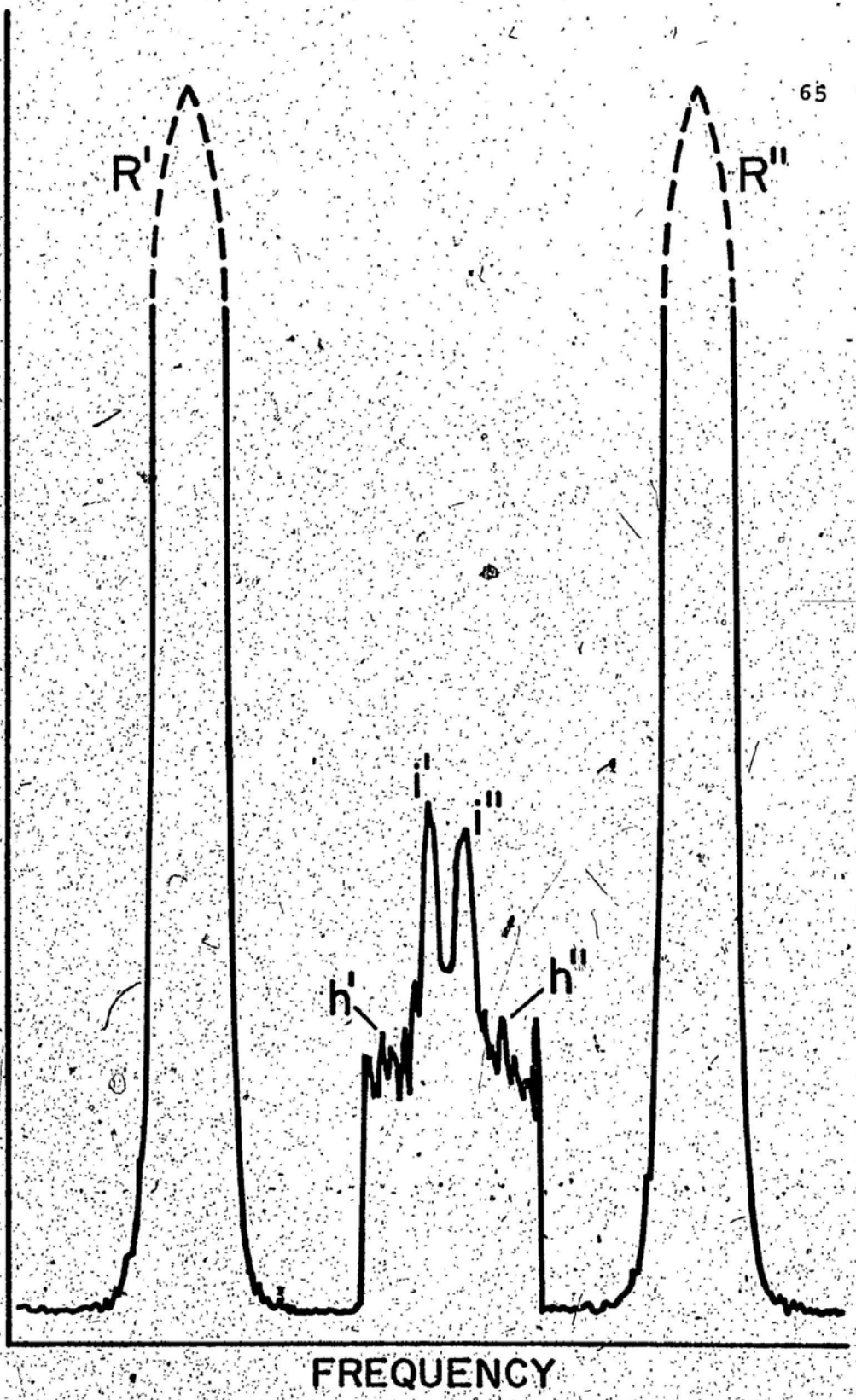

Fig. 4.10 Xenon Hydrate: Spectrum IVB

Fig. 4.11 Xenon Hydrate: Spectrum IVC

increase in the hydrate to ice count rate. Attenuation of the laser beam in the hydrate, as evidenced by the parasitic scattering, could account for the loss of the hydrate peaks.

IV.1.2. Samples 1-4: Frequency Shift Determination

Table 2 lists the channel positions of the ice (i) and xenon hydrate (h) peaks of those spectra from the first four xenon hydrate samples pertinent to the determination of the frequency shift. To summarize, IB and IC were taken at different heights (by rotating the glass plate) in the same hydrate sample; sets IIA, IIB and IIIA, IIIB were taken at different regions in a new hydrate sample and IVA, IVB and IVC were taken after further growth of the sample already present. All four regions are treated independently in the calculations.

Placed in brackets after the channel numbers of the hydrate peaks is the estimated uncertainty, in channel numbers, of the position of the peak. In some cases, this uncertainty arose because of the lack of a well-defined 'peak' despite the fact that the signal itself was quite prominent (e.g., IB). Uncertainty also arose in proportion to the significance of the random nature of the background count for each channel, both in cases where the hydrate signal was weak (IIIA) and for spectra of short accumulation time (IVA). No uncertainty was stated for the position of the ice peaks as these were quite well defined. In any event, any error here would be negligible in comparison to the error in the hydrate signal position.

Table 2: Xenon Hydrate & Ice: Channel Displacement Data

	Channel Position		Channel Displacement		
Spectrum	Ice	Hydrate	Central-Ice	Central-Hydrate	Ice-Hydrate
IB	337	322(1)	87	72	15
	354	369(1)	93	78	15
IC	337	322(1)	87	72	15
	355	370(1)	93	78	15
IIA	340	324(1)	90	74	16
	354	372(2)	94	76	18
IIIA	340	323(1)	90	73	17
	355	369(1)	93	79	14
IVA	340	323(2)	90	73	17
	354	369(2)	93	78	15
IVB	340	325(1)	90	75	15
	354	369(2)	93	78	15

Spectrum	Channel Displacement	Weighting Factor
IB, IC	15	10
IIA	17	2.5
IIIA	15.5	2
IVA, IVB	15.5	4

Average Channel Displacement = 15.4

Normally, the frequency shift for xenon hydrate would be determined directly from the channel displacements h"-R" and R'-h'. For several reasons, it was decided not to do this here. First of all, a slight non-linearity existed between the channel number and the separation of the plates of the Fabry-Perot. This is evidenced by the location of the central peaks (in most cases) at channels 47, 250 and 448. The problem was enhanced with the use of the (69 channel) segmented time base between the second and third central lines. Typically, without the segment, the shifts between the ice peaks and the respective central peaks differed at most by two channels. However, when using the segment, a discrepancy in the shifts of up to six channels (see IB) was recorded. After the data of Table 2 had been collected, it was observed, using a new ice crystal, that the channel position of the two ice peaks between the second and third central lines shifted by about three channels towards the second Rayleigh. This resulted in a shift discrepancy of six channels, whereas without the segment, the ice peaks were symmetrically located. However, the average shift remained identical to the two equal displacements determined without the segment. This implied that the increased non-linearity imposed by the segment did not occur within the segment itself. This is probably related to an inability of the Fabry-Perot plates to respond exactly to the instructions stipulated by the DAS immediately prior to, and following, imposition of the segment.

An attempt was not made to compensate for the adverse effects of the segment. Rather, the frequency shift of the hydrate was, as noted, determined relative to the ice signal. Using the data of Gammon (Ph.D. Thesis) a shift of 91.2 channels from the central component would be most probable for ice. The average displacement for the first ice crystal was 90.0 channels, and 91.6 for the second. The discrepancy for this data is most likely due to the growth of ice crystals of significantly different orientations.

It is evident that for most spectra, there is excellent agreement between the two values of the channel displacement between the ice and hydrate signals (i"-h" and h'-i') for each spectrum. This is particularly the case for IB and IC. It is recalled that these spectra contained the strongest hydrate signals, with the longest accumulation times. On the other hand, the spectra of regions II, III and IV were of much shorter accumulation times and contained weaker hydrate signals. As such, some discrepancy is apparent between the two channel displacements in the spectra. However, the data is considered sufficiently reliable to be used in the calculations.

Because of the varying degrees of reliability, each spectrum has been assigned a weighting factor for use in averaging the displacement between the ice and hydrate signals. An arbitrary value of 10 was assigned to region I. Subsequent spectra were then assigned weighting factors as decided by the intensity of the hydrate signal and accumulation time.

The results of spectra IVA and IVB are presented together, with an average displacement of 15.5 channels. The resultant average displacement between the ice and hydrate signals is 15.4 channels (Table 2). This value is assumed accurate within a two channel range. Despite the unambiguous position of the ice signal in nearly all spectra, one channel error is assigned here, as well, to allow for the slight discrepancy of the recorded ice signal position with the signal corresponding to the average sound velocity. A value of 3845 m/s (Gammon, Ph.D. Thesis) is used as the average longitudinal velocity of sound. Using the Brillouin equation, this corresponds to a 91.2 channel displacement from the central peak. Hence, the fractional reduction in the frequency shift of xenon hydrate relative to ice (for this series of spectra) is 15.4/91.2 = .169± .011.

IV.1.3. Sample 5: Spectra and Frequency Shifts

The majority of spectra taken of the final xenon hydrate sample, listed in order of increasing cell height, are shown in Figs. 4.12-4.17. These include observation within the ice crystal (Figs. 4.12, 4.13), the poorer quality hydrate, or discontinuity between ice and transparent hydrate, (Fig. 4.14) and within the transparent hydrate (Fig. 4.15-4.17). The glass plate position necessary to view the poor quality hydrate was easily determined by the fact that much laser scattering occurred

at this region, thereby resulting in a high central component in the spectrum. The plate rotation angle of 15° for this region, being close to the vertical position, agrees with the fact that the He-Ne beam, defining the optic axis, passed through this region. Fig. 4.15 represents the strongest hydrate signal, while spectra taken at lower and higher cell positions exhibited reduction in the signal intensity, as expected. Only the ice signal was observed below the discontinuity, while above the discontinuity only the hydrate signal was present.

Table 3 lists some of the pertinent spectral data for this series of spectra. The glass plate positions are only approximate, having been judged visually. Note that the incident laser intensity for the first two spectra was three times that for subsequent spectra, the lower power being about 70 mW.

Table 3: Data for Sample 5: Xenon Hydrate Spectra

Spectrum	Glass Plate Rotation Angle	Accumulation Time Per Segmented Ch. (Sec)	Hydrate or Ice Signal Rate (CTS/sec)	BKGD. Rate (CTS/s)
V1*	-20°	127.5	7.0	2.6
V2*	+5°	248.2	3.1	5.9
V3	15°	670.8	—	2.0
V4	45°	326.8	2.1	1.9
V5	50°	570.5	0.9	1.9
V6	55°	673.5	0.4	2.0

*Laser power three times more intense than subsequent.

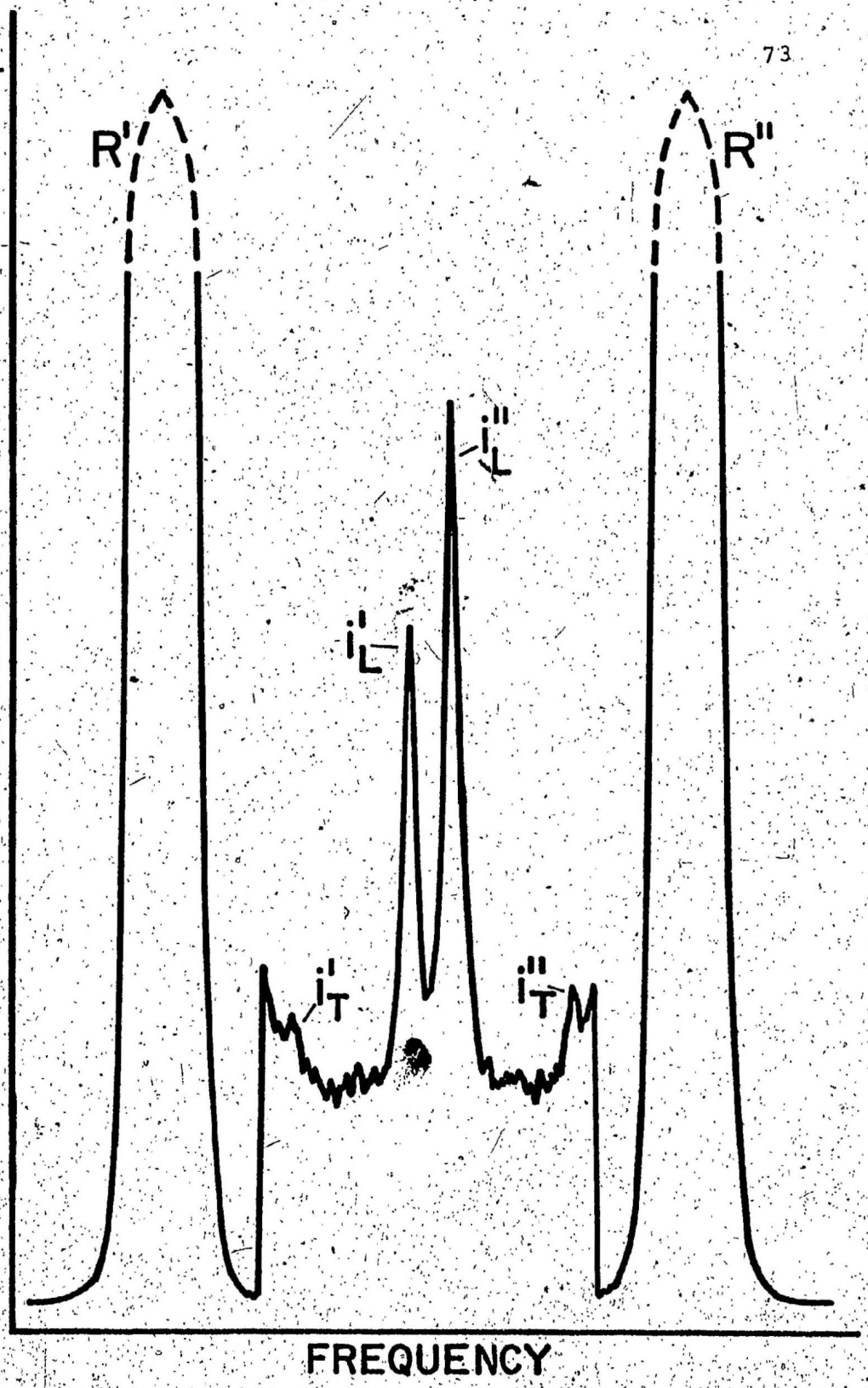

Fig. 4.12 Xenon Hydrate: Spectrum VI

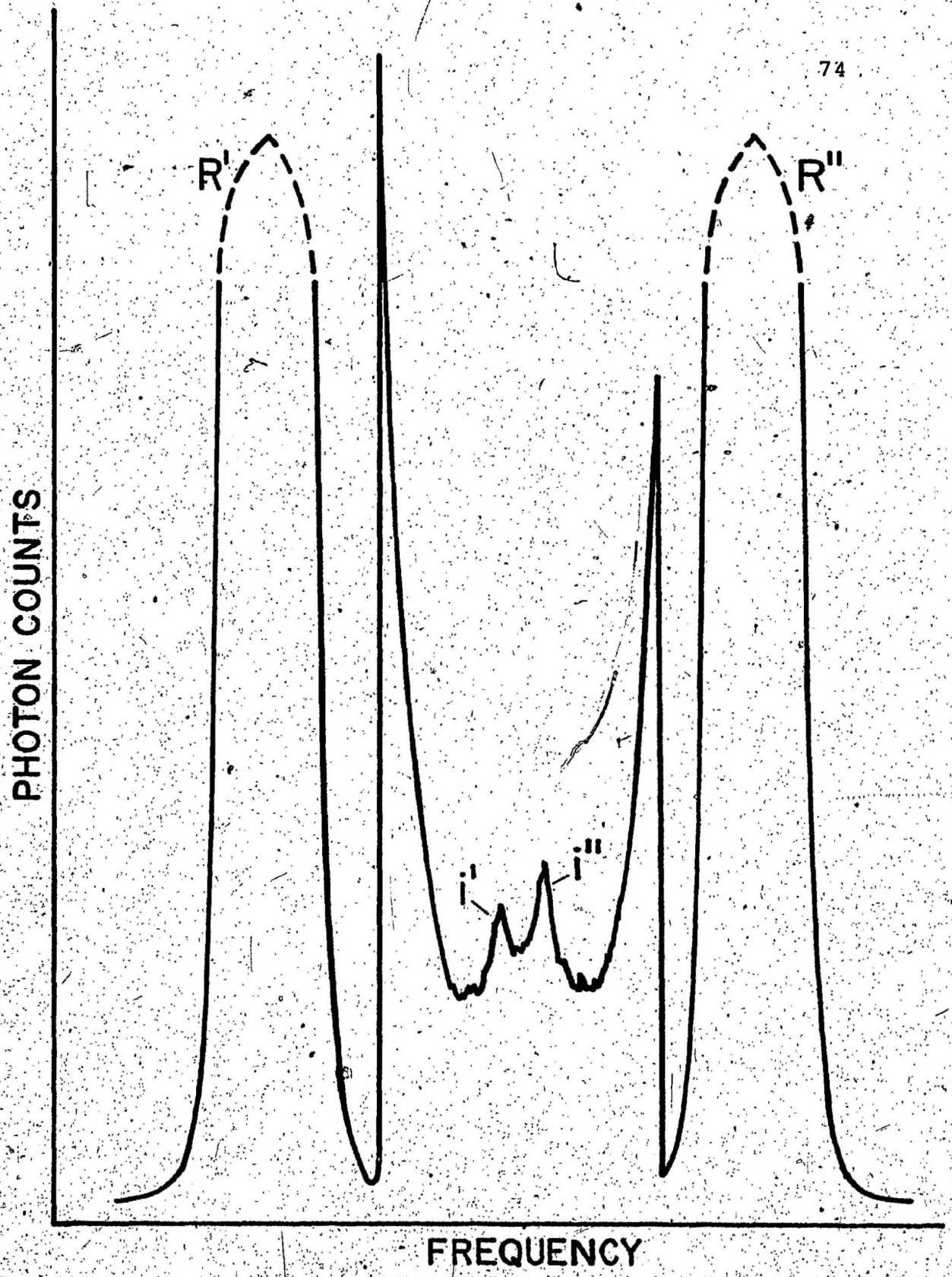

Fig. 4.13 Xenon Hydrate: Spectrum V2

Fig. 4.14 Xenon Hydrate: Spectrum V3

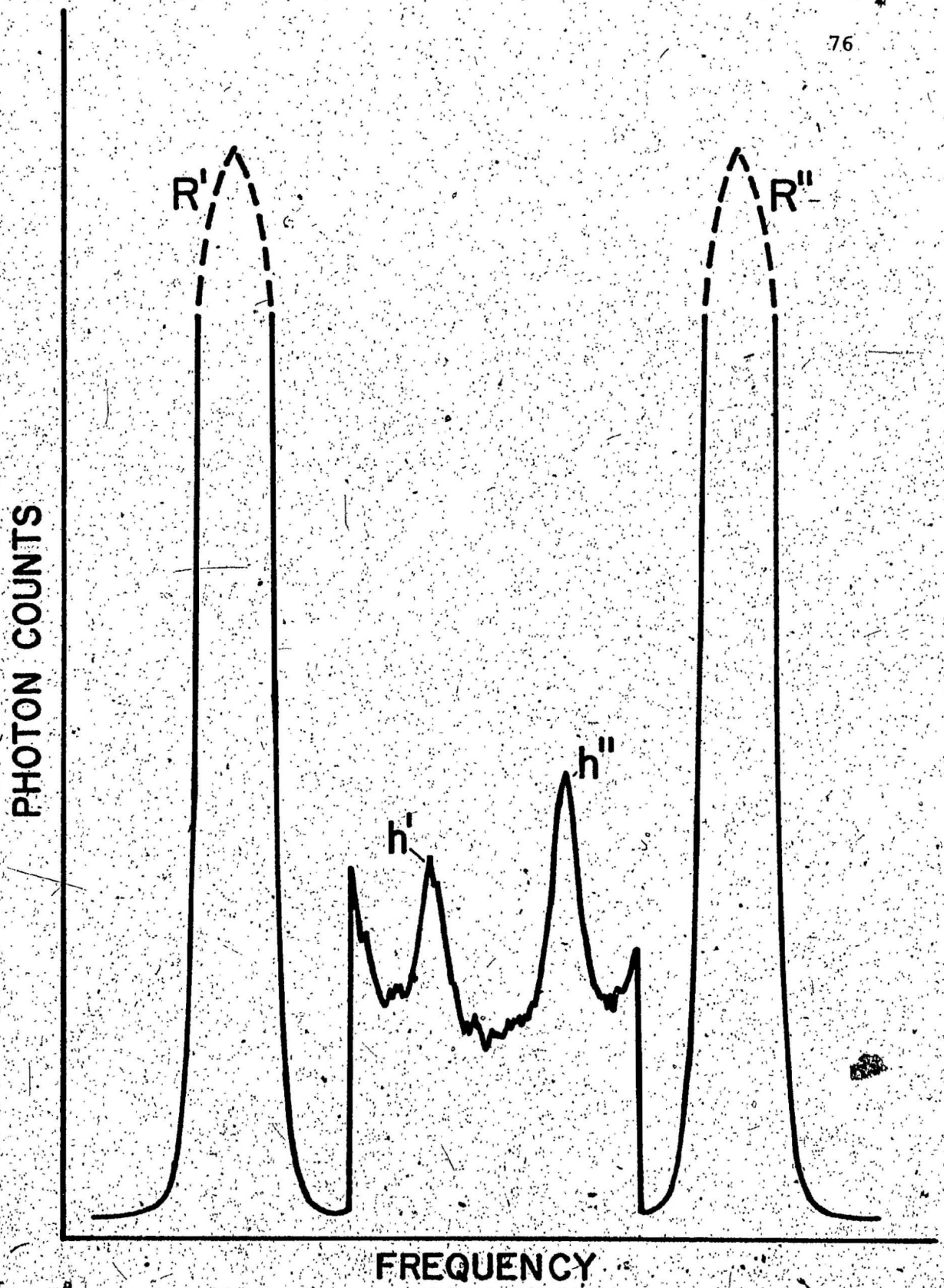

Fig. 4.15 Xenon Hydrate: Spectrum V4

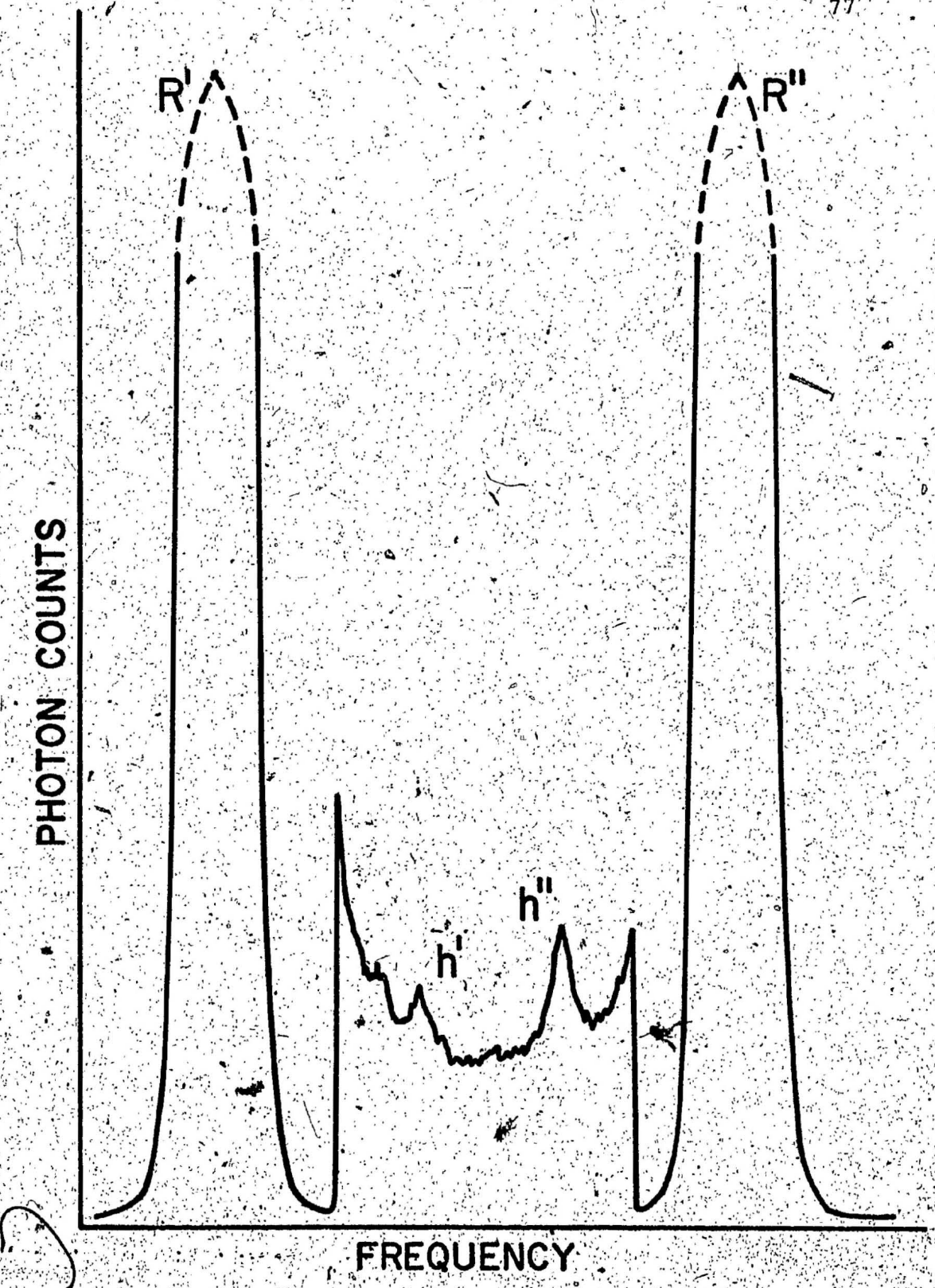

Fig. 4.16 Xenon Hydrate: Spectrum V5

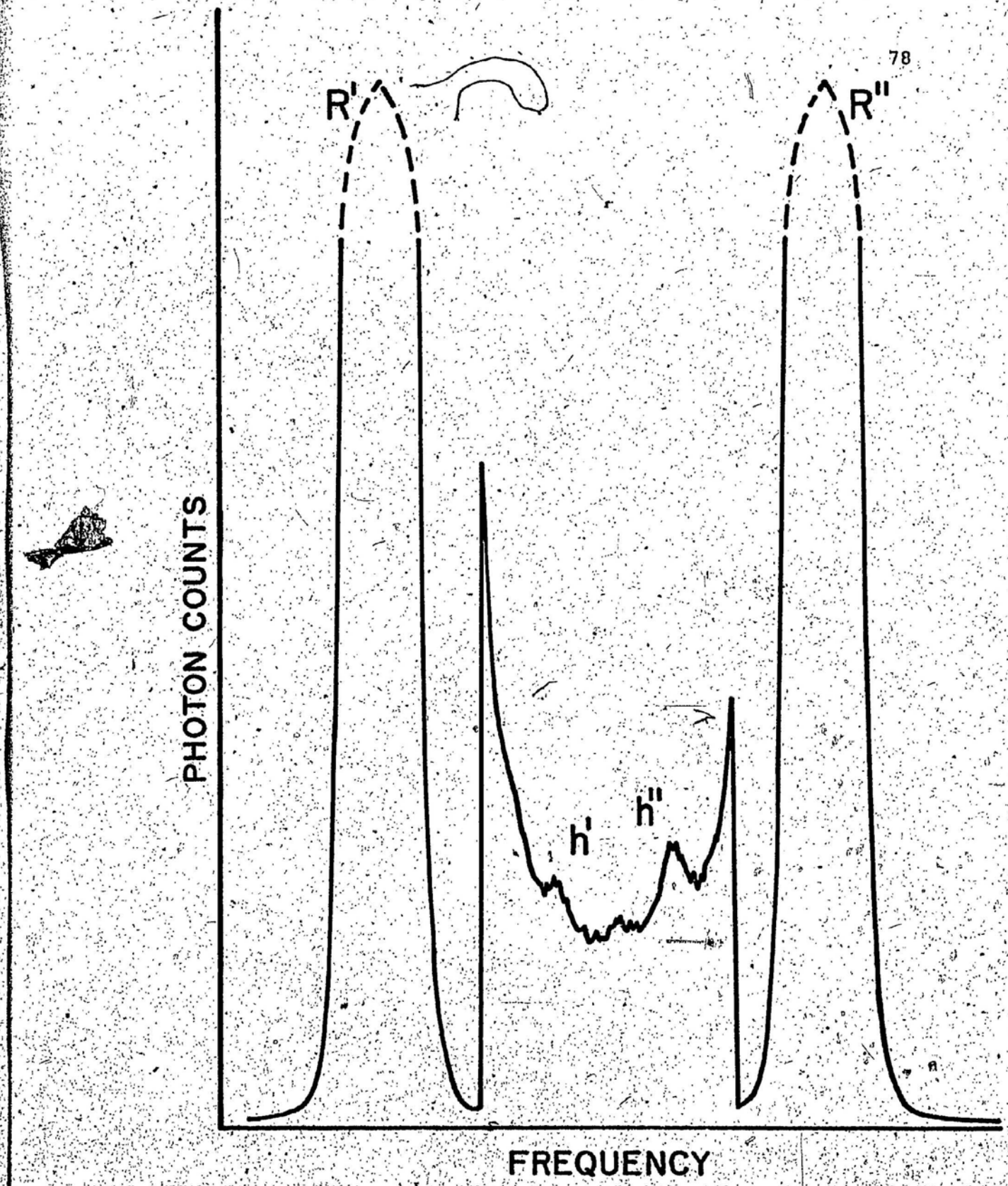

Fig. 4.17 Xenon Hydrate: Spectrum V6

The positions of the longitudinal signals of both the ice and hydrate samples varied somewhat between different spectra, although no direct correlation with cell position observed was evident. The channel positions varied from 337-338 and 352-354 for the ice signal, and 317-318.5 and 369.5-371 for the hydrate. Hydrate values of 318 and 370 were used in the calculations, as based on the average of all spectra, with extra weighing on those spectra containing the strongest signals (317.5,371 and 318,370). Using channel positions of 338 and 354 from the best ice spectrum, the channel displacements between the ice and hydrate signals were 20.5 and 16. This yields an average displacement of 18.25±2 channels. The average observed ice shifts agreed well with the most probable value (as noted earlier), thereby justifying the use of the ice signal positions in calculating the sound velocity ratio between ice and hydrate. Again assuming an error range of one channel in the ice signal, the frequency shift of xenon hydrate relative to ice, for this sample is 18.25/91.2 = .200±.022. The source of the 4.5 channel discrepancy between the pair of ice-hydrate displacements is not clear. Without further knowledge concerning this difficulty, a simple averaging of the results would appear to be the only solution.

IV.1.4. Longitudinal Sound Velocity Ratio

The sound velocity in xenon hydrate was determined relative to the velocity in ice. Applying the Brillouin equation to both substances, and then dividing one by the other, yields

$$\frac{V_h}{V_i} = \frac{n_i}{n_h} \cdot \frac{\Omega_h}{\Omega_i} \qquad 4.1$$

where V is the velocity, n is the refractive index and Ω is the frequency shift. The values for the fractional reduction in the frequency shifts of xenon hydrate relative to ice are equal to $1 - \Omega_h/\Omega_i$.

The index of refraction of xenon hydrate was determined using the Lorentz-Lorenz relation

$$\frac{4\pi n\alpha_h}{3} = \frac{n^2-1}{n^2+2} \qquad 4.2$$

where n is the number density of the hydrate, α is the polarizability per molecule and n is the refractive index. The polarizability of the hydrate was calculated via summation of the fractional contributions from the water molecule and xenon atom. The polarizability of xenon was determined from Equation 4.2 using liquid phase values of ρ = 2.857 g/cm^3 and n = 1.376 ± .001 (Sinnock, 1969), yielding α_{Xe} = 4.18(±.01) x 10^{-24} cm^3. Similarly, using the ice values n = 1.312 ± .001 (International Critical Tables, 1926-33) and ρ = 0.9175 ± .015 (Gammon, 1980), the H_2O polarizability was calculated to be α_{H_2O} = 1.51(±.02) x 10^{-24} cm^3. From these values, the polarizability of xenon

hydrate (a_h) was calculated at cage occupancies of 75%, 90% and 100%. Corresponding values for the number densities were calculated using a value of 11.97 Å ± 0.03 (von Stackelberg, 1954) as the lattice constant for xenon hydrate. This value was also used to determine the hydrate densities listed in Table 4. The resultant indices of refraction, n_h, as calculated using Equation 4.2 (listed in order of increasing cage occupancy) are 1.38, 1.40 and 1.42 (±.005).

Two sets of sound velocity ratios are listed -- one for the average of the two frequency shift ratios calculated ($\frac{.200 + .169}{2}$ = .185 ± .016) and one for the ratio (.200 ± .022) determined from the final sample. The sound velocity ratios are

For $\frac{\Omega_h}{\Omega_i}$ = .815	V_h/V_i (±.016)	Cage Occupancy (%)
	.775	75
	.764	90
	.753	100

For $\frac{\Omega_h}{\Omega_i}$ = .800	V_h/V_i (±.022)	Cage Occupancy (%)
	.761	75
	.750	90
	.739	100

IV.2. Methane Hydrate Spectra and Sound Velocity Ratio

Only two spectra (Figs. 4.18-4.19) taken of the methane hydrate samples contained longitudinal hydrate signals sufficiently intense to be used in the sound velocity calculations, although the translational shift of the ice peaks were evident. The channel displacements from the ice signals were 5.5 and 8 for the first spectrum, and ten channels for each pair in the second. Although these differences appear quite pronounced when expressed in this manner, one should bear in mind that if the frequency shifts were calculated in the conventional manner (i.e., relative to the central lines), the hydrate signals displaced 5.5 and ten channels from the ice signals would differ in frequency shift by only 5%.

The average channel displacement, 8.4 channels, was used to calculate the velocity ratios. Using the calculated channel displacement for the average sound velocity in ice for these spectra, the frequency shift ratio is $\Omega_h/\Omega_i = .906 \pm .022$. Errors of ± two channels and ± one channel are given for the hydrate and ice signals respectively.

A similar procedure as outlined for xenon hydrate was used to determine the refractive indices of methane hydrate at the different occupancies. Values of $n = 1.323 \pm .005$ and $\rho = 0.4874\ g/cm^3 \pm .0015$ (Rand, 1978) for solid methane gave a polarizability value $\alpha = 2.60(\pm.03) \times 10^{-24}\ cm^3$. The number densities were calculated using a value of 12.03 Å ± .06 (Davidson, 1973) as the lattice constant of methane hydrate.

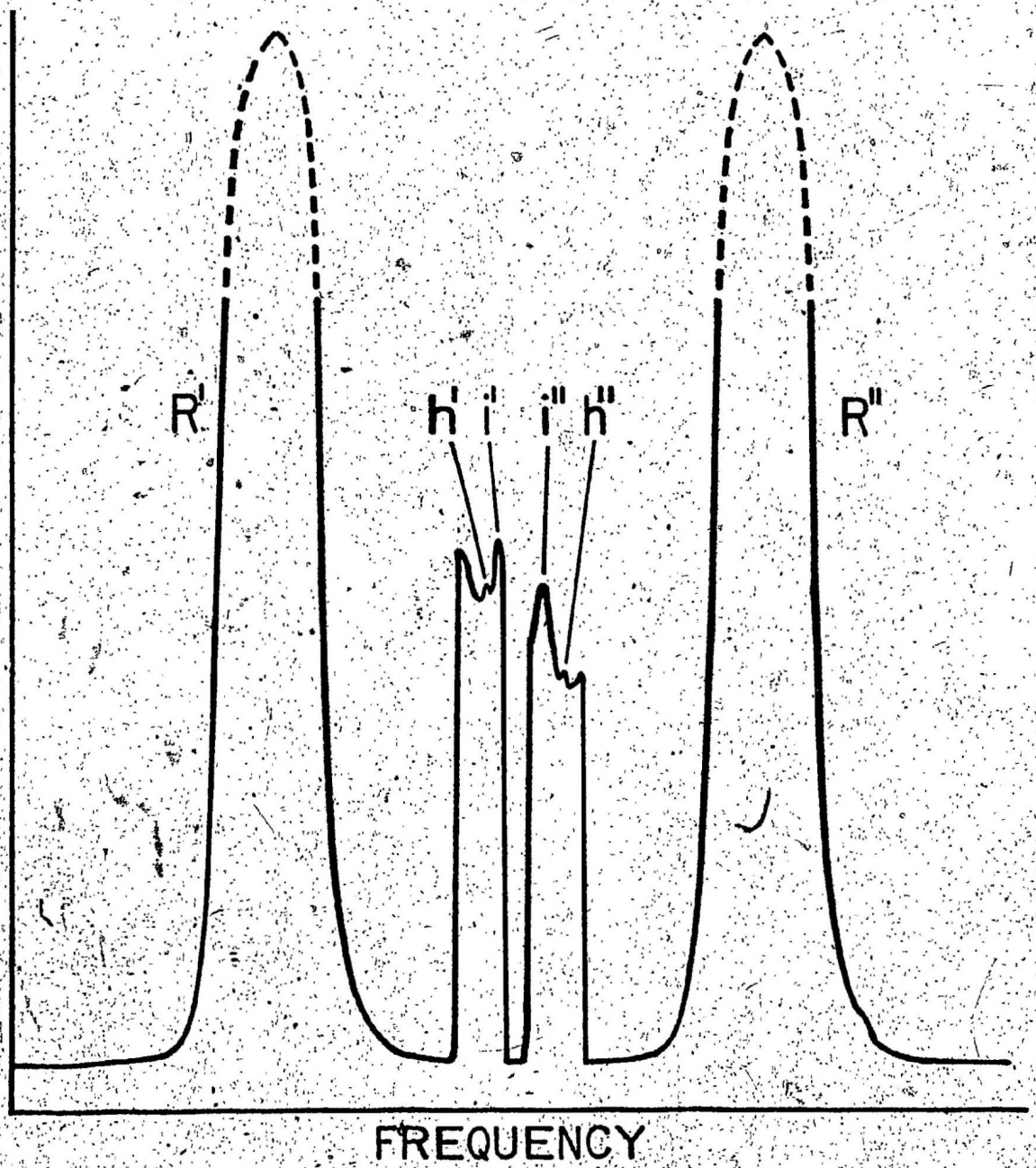

Fig. 4.18 Methane Hydrate

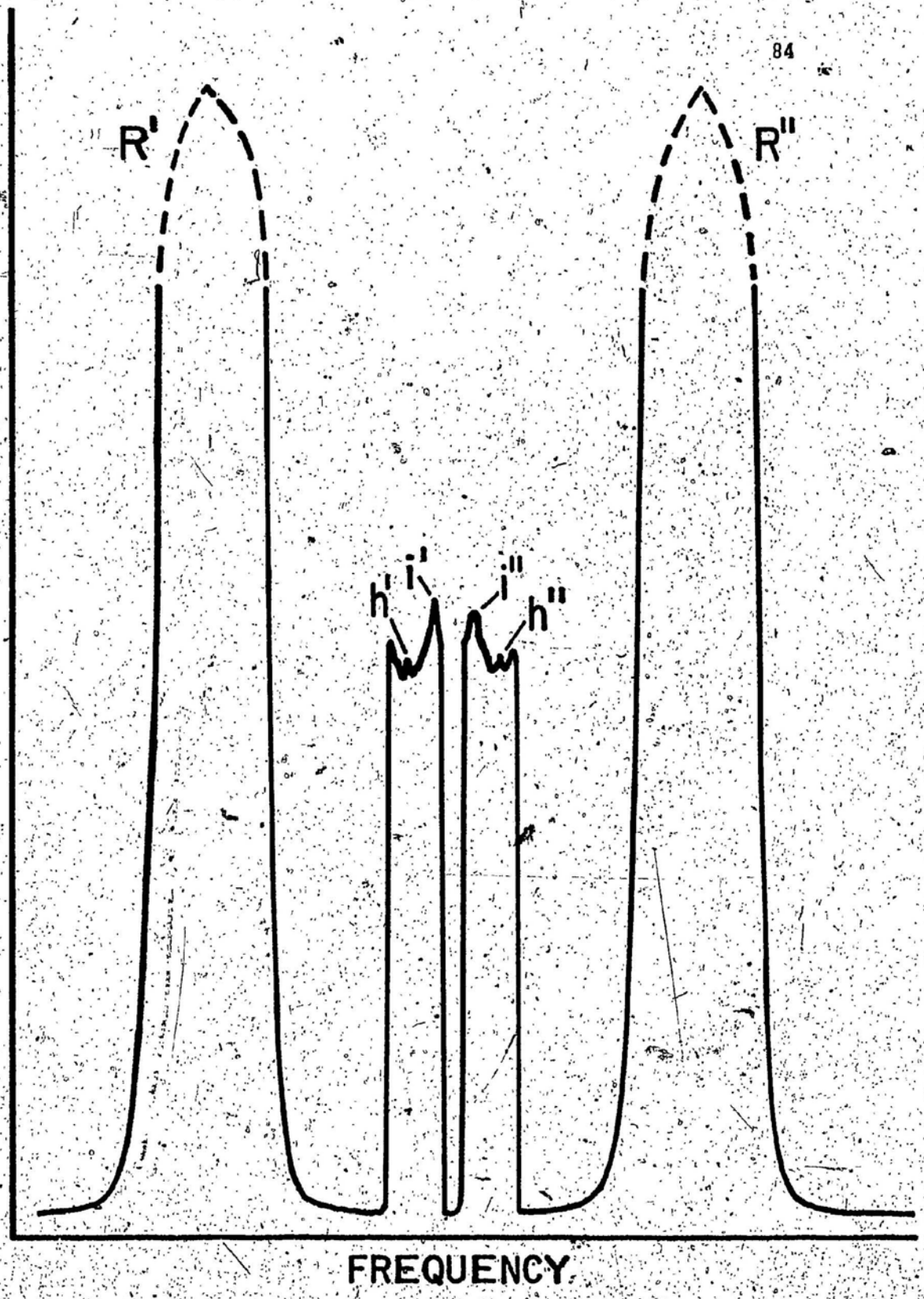

Fig. 4.19 Methane Hydrate

The resultant indices of refraction of methane hydrate at 75%, 90% and 100% occupancies are 1.33, 1.34, and 1.35 (±.01). The corresponding sound velocity ratios are

V_h/V_i (±.025)	Cage Occupancy (%)
.894	75
.887	90
.880	100

V. DISCUSSION

V.1. Comparison of Results with Previous Work

To date, the only theoretical calculation to predict longitudinal sound velocities in hydrates was carried out by Whalley (1980). The derivation of the final equation begins with the standard expression for the velocity V, in an infinite isotropic medium:

$$V^2 = E\,(1-\nu)/\rho\,(1+\nu)\,(1-2\nu) \qquad 5.1$$

where E and ν are respectively Young's modulus and Poisson's ratio. From elasticity theory for an isotropic medium, it may be shown that Young's modulus is related to the adiabatic Bulk modulus B, by

$$B = \frac{1}{K_s} = E/3\,(1-2\nu) \qquad 5.2$$

where K_s, the adiabatic compressibility, is, by definition, the reciprocal of the Bulk modulus. Upon substitution of the thermodynamic relation

$$\frac{K_s}{K_t} = 1 - \frac{\alpha^2 TV}{K_t C_p} \qquad 5.3$$

into Equation 5.2, followed by substitution into Equation 5.1, to eliminate E, the following relation is obtained.

$$V^2 = \frac{3}{K_t} \cdot \frac{1}{\rho} \cdot \frac{1-\nu}{1+\nu} \cdot \frac{1}{1-\frac{\alpha^2 Tv}{K_t C_p}} \qquad 5.4$$

Applying Equation 5.4 to both ice and hydrate and dividing one by the other, yields the final result:

$$\frac{V_h^2}{V_i^2} = \frac{K_{ti}}{K_{th}} \cdot \frac{\rho_i}{\rho_h} \cdot \frac{1-\nu_h}{1-\nu_i} \cdot \frac{1+\nu_i}{1+\nu_h} \cdot \frac{1-\alpha_i^2 Tv_i/K_{ti}C_{pi}}{1-\alpha_h^2 Tv_h/K_{th}C_{ph}} \qquad 5.5$$

V = longitudinal velocity
K_t = isothermal compressibility
ρ = density
ν = Poisson's ratio
T = temperature
v = molar volume
Cp = heat capacity
α = volume thermal expansivity

Assuming 100% cage occupancy, respective velocity ratios $(\frac{Vh}{Vi})$ of .939 and .945 were obtained for methane hydrate and propane hydrate at 0°C. An attempt is made here to use this equation to yield theoretical values of $\frac{Vh}{Vi}$ for cage occupancies of 75%, 90% and 100% for methane and xenon hydrate at -10°C.

Whalley's calculations for Structure I required the following data and assumptions: $\nu_i = \nu_h$, $K_{ti} = 12 \text{Mbar}^{-1}$, $K_{th}/K_{ti} = 1.135$, $\alpha_i = \alpha_h = 1.5 \times 10^{-4} K^{-1}$, $C_{pi} = 37.7 \text{J/kmol}$ and

ρ_i = 0.9181 g/cm^3 (corrected to -10°C, from Butkovich, 1958). The assumed heat capacity contribution from the guest molecules was 3R and 3R/2 (for methane hydrate only) for vibrational and rotational motion respectively. Density values of .790 g/cm^3 and .802 g/cm^3 for the empty methane and xenon hydrate lattices were used to determine hydrate densities at the various cage occupancies. The molar volume v_i was not given but was calculated to be 1.97 x 10^{-5} m^3/mol.

Table 4: Comparison of Theoretical Xenon and Methane Hydrate Velocity Ratios with Experimental Values

Guest Molecule	Cage Occ. (%)	ρ_{h_3} g/cm^3	C_{ph} J/K·mol	V_h/V_i Theor.	Expt.	
Xe	75	1.564	40.9	.718	.775	.761
	90	1.717	41.6	.686	.764	.750
	100	1.818	42.0	.666	.753	.739
CH_4	75	.8821	42.6	.956	.894	
	90	.9004	43.6	.946	.887	
	100	.9127	44.2	.940	.880	

The calculated hydrate molar volumes (xenon hydrate: v_h = 2.25 x 10^{-5} m^3/mol, methane hydrate: v_h = 2.28 x 10^{-5} m^3/mol) were independent of the cage occupancy. In considering the various occupancies, then, only the heat capacity contribution by the guest molecules and the densities need to be accounted for. The exact heat capacity differences are not of great

concern, as the maximum difference in the last term of eqn. 5.5 throughout the calculations was less than 0.1%. The values in Table 6 are calculated at -10°C to correspond with the hydrate temperature in the present experiment. Also included in Table 4 is a comparison with the experimental values and percentage discrepancies for methane hydrate and the two sets of data for xenon hydrate.

Whalley's results may also be compared with the experimentally determined sound velocities of propane hydrate (Structure II) by Pandit and King (1981). Using ultrasonic techniques, longitudinal velocities of 3.18 km/s and 3.05 km/s for the two propane hydrate specimens (ρ = .850 g/cm^3 and .750 g/cm^3) and 3.80 km/s for ice were reported, with an average hydrate: ice ratio of .820. Eqn. 5.1, however, yields a ratio of .945, as reported by Whalley for a propane hydrate sample (ρ = .883 g/cm^3) of full occupancy at 0°C. Use of Pandit's density measurements in eqn. 5.1 (rather than the density at full occupancy) yields even higher calculated hydrate: ice ratios.

V.2. Summary

The longitudinal acoustic velocities of methane and xenon hydrate have been determined with (limited) success. Clearly, a major part of the effort in this work was the production of suitable samples. The final xenon hydrate sample, having yielded the most intense Brillouin signals, shall be

used as a guide in the following discussion of the most suitable growth procedures.

As in all other spectroscopically-studied samples, growth of the final xenon hydrate sample entailed pressurizing the cell with the gas above a single ice crystal. In addition to hydrate formation within the crystal, further hydrate growth, for the last sample, continued above the ice crystal via combination of water vapor (trapped in the system) and xenon gas. As was explained (Sect. III.2.), the beam readily passed through this hydrate sample, and relatively intense longitudinal hydrate signals were easily obtained.

In all previous cases, the hydrate samples obtained through direct inclusion of the gas into the ice crystal were relatively opaque to the laser beam. This was evidenced by the tremendous amount of scattering prevalent at the ice-hydrate boundary and created numerous problems related to obtaining a Brillouin signal independent of the poor hydrate quality itself. First of all, poor beam penetration implied reduced Brillouin scattering due to attenuation of the beam, with a resultant greater need for precision optical alignment. As well, the scattering at the boundary not only increased the background of the Brillouin spectra (of particular concern in view of the weak hydrate signals), but also required further reduction of the laser power to avoid overloading of the photomultiplier tube. Finally, it is possible that attenuation of the beam at the boundary may have caused localized destruction of the hydrate.

Evidently, the most suitable method of xenon hydrate growth is formation from xenon gas and water vapor, each supplied from an external reservoir. The presence of an ice crystal, as a catalyst for hydrate formation, may also be a requirement, though this has not been established. The hydrate obtained required about two days to grow, and was of reasonable quality. Growth of a better sample, possibly even a single crystal, would appear to require no more than a refinement of the growth process. This would involve growth at different xenon gas pressures, cell temperatures and the concentration of water vapor in the cell. The latter may well be the most influential as far as growth rate, and therefore, sample quality, is concerned. In any case there is certainly cause for optimism with respect to further study.

Both methods employed to obtain the methane hydrate samples (i.e., (1) flow of methane gas and water vapor through the cell, and (2) direct inclusion of static methane gas into the ice crystal) are viewed as having been successful in obtaining bulk quantities. Although Brillouin signals were obtained only from samples grown using the latter method, it is felt that refinements to the former procedure offer the most promise for production of more suitable samples. Especially in view of the results of xenon hydrate growth, possible improvements include: (1) a reduction, or variable control, in the concentration of water vapor in the methane gas, (2) thermal insulation, or heating of the hypodermic to avoid blockage resulting from

hydrate formation and (3) refinements of the gas handling system to permit the use of higher methane gas pressures.

Nearly all spectra of both methane and xenon hydrate samples were plagued by very low longitudinal hydrate signals -- a problem whose origin was directly a result of the samples' poor optical quality. (Precision optical alignment was, in all cases, ensured by the intense ice signals). On numerous occasions throughout the course of the experiment, no Brillouin signals from the hydrates could be obtained. In most other cases, the signals were so weak as to cause difficulty in establishing the correct channel positions of the signals. This difficulty has been illustrated for xenon hydrate in Table 2, where, for some spectra, the displacements between the ice and hydrate signals differed by as much as three channels, and for methane hydrate in Sect. IV.2., where a maximum discrepancy of almost five channels is noted. The results listed in Table 2 for the first four samples of xenon hydrate are reasonably consistent. The discrepancy between these results and those of the last sample probably arose from differences in sample quality. The data presented for methane hydrate is felt to be insufficient.

Approximate agreement is evidenced between the experimental results and those obtained through Equation 5.5. For methane hydrate, the theoretical results were about 6% greater and for xenon hydrate about 10% lower. Reconsideration of the assumptions used in the theoretical model may give rise to better agreement.

REFERENCES

Barrer, R.M. and W.I. Stuart, Proc. Roy. Soc. A, 242, 172 (1957).

Barrer, R.M. and D.J. Ruzicka, Trans. Far. Soc., 58, 2262 (1962).

Barrer, R.M. and A.V.J. Edge, Proc. Roy. Soc. (London) A, 300, 1 (1967).

Benedek, G.B. and K. Fritsch, Phys. Rev., 149, 647 (1966).

Bily, C. and J.W.L. Dick, Bull. Can. Petrol. Geol., 22, 340 (1974).

Born, M. and K. Huang, Dynamical Theory of Crystal Lattices (Clarendon Press, Oxford, 1954).

Butkovich, T.R., J. Applied Physics, 30, 350 (1958).

Chersky, N. and Y. Makogon, Oil Gas Invest., 10, 82 (1970).

Claussen, N.F., J. Chem. Phys., 19, 662 (1951).

Davidson, D.W., in: Water, A Comprehensive Treatise, vol.2, edited by F. Franks (Plenum Press, New York, 1973).

Davy, H., Phil. Trans. Roy. Soc. (London), 101, 1 (1811).

Deaton, W.M. and E.M. Frost, U.S. Bur. Mines, Monograph 8 (1946).

Faraday, M., Quart. J. Sci., 15, 71 (1823).

Gammon, P.H., M. Sc. Thesis, Memorial University of Newfoundland, 1978 (Unpublished).

Gammon, P.H., H. Kiefte, and M.J. Clouter, J. Glaciol., 25, 159 (1980).

Gammon, P.H., Ph. D. Thesis, Memorial University of Newfoundland, 1981 (Unpublished).

Hammerschmidt, E.G., Ind. Eng. Chem., 26, 851 (1934).

Holder, G.D., Ph. D. Thesis, University of Michigan, 1976.

International Critical Tables (McGraw-Hill Book Co., New York and London, 1926-1933).

Jeffrey, G.A., Accounts Chem. Res., 2, 344 (1969).

Katz, D.L., in: Handbook of Natural Gas Engineering (McGraw-Hill Book Co., New York, 1959).

Kobayashi, R., H.J. Withrom, and G. Williams, Nat. Gas Assoc. Amer., p. 47 (1955).

McKoy, V. and O. Sinanoglu, J. Chem. Phys., 38, 2946 (1963).

Miller, S.L., Proc. Natl. Acad. Sci., 47, 1798 (1961).

Miller, S.L., Science, 165, 489 (1969).

Miller, S.L., in: Physics and Chemistry of Ice, edited by E. Whalley, S.J. Jones, and L.W. Gold (Royal Society of Canada, Ottawa, 1973).

Nagata, I. and R. Kobayashi, I. & E.C. Fundam., 5, 466 (1966).

Pandit, B.I. and M.S. King, paper presented at the Fourth Canadian Permafrost Conference, Calgary, March, 1981.

Pauling, L. and R.E. Marsh, Proc. Nat. Acad. Sci., 38, 112 (1952).

Powell, H.M., J. Chem. Soc. (London), 61, (1948).

Rand, S.C., Ph. D. Thesis, University of Toronto, 1978.

Roberts, C.L., E.R. Brownscombe, and L.S. Howe, Oil and Gas Journal, 39, 36 (1940).

Sinnock, A.C. and B.L. Smith, Phys. Rev., 181, 1297 (1969).

Stackelberg, M. von and H.R. Muller, Naturwiss., 39, 20 (1952).

Stackelberg, M. von and H.R. Muller, Z. Electrochem., 58, 25 (1954).

Staveley, L.A.K., in: Non-Stoichiometric Compounds, edited by L. Mandelcorn (Academic, New York, 1964).

Stoll, R.D., J. Ewing and G.M. Bryan, J. Geophys. Res., 76, 2090 (1971).

Stoll, R.D. and G.M. Bryan, J. Geophys. Res., 84, 1629 (1979).

Tester, J.W., R.L. Bivins, and C.C. Herrick, A.I. Ch. E. Journal, 18, 1220 (1972).

Waals, J.W. van der, and J.C. Platteeuw, Adv. Phys. Chem., 2, 1 (1959).

Whalley, E., J. Geophys. Res., 85, 2539 (1980).

Whipple, F.L., Astrophys. J., 113, 464 (1951).